

1 **High-resolution Crystal Structures of Transient Intermediates in the Phytochrome**
2 **Photocycle**

3 Melissa Carrillo¹, Suraj Pandey², Juan Sanchez¹, Moraima Noda¹, Ishwor Poudyal², Luis Aldama¹,
4 Tek Narsingh Malla², Elin Claesson³, Weixiao Yuan Wahlgren³, Denisse Feliz¹, Vukica Šrajer⁴,
5 Michal Maj³, Leticia Castillon³, So Iwata^{5,6}, Eriko Nango^{6,7}, Rie Tanaka^{5,6}, Tomoyuki Tanaka^{5,6},
6 Luo Fangjia^{5,6}, Kensuke Tono^{6,8}, Shigeki Owada^{6,8}, Sebastian Westenhoff^{3*}, Emina A.
7 Stojkovic^{1*} and Marius Schmidt^{2*}

8

9 ¹ *Department of Biology, Northeastern Illinois University, 5500 N. St. Louis Ave., Chicago, IL, 60625*
10 *USA*

11 ² *Physics Department, University of Wisconsin-Milwaukee, 3135 N. Maryland Ave., Milwaukee, WI,*
12 *53211 USA*

13 ³ *Department of Chemistry and Molecular Biology, University of Gothenburg, Box 462, 40530*
14 *Gothenburg, Sweden*

15 ⁴ *The University of Chicago, Center for Advanced Radiation Sources, 9700 South Cass Ave, Bldg 434B,*
16 *Argonne, IL 60439, USA*

17 ⁵ *Department of Cell Biology, Graduate School of Medicine, Kyoto University, Yoshidakonoe-cho, Sakyo-*
18 *ku, Kyoto, 606-8501, Japan*

19 ⁶ *RIKEN SPring-8 Center, 1-1-1, Kouto, Sayo-cho, Sayo-gun, Hyogo 679-5148, Japan*

20 ⁷ *Institute of Multidisciplinary Research for Advanced Materials, Tohoku University, 2-1-1*
21 *Katahira, Aoba-ku, Sendai 980-8577, Japan*

22 ⁸ *Japan Synchrotron Radiation Research Institute, 1-1-1 Kouto, Sayo-cho, Sayo-gun, Hyogo 679-5198,*
23 *Japan*

24 **corresponding authors*

25 *Correspondence: sebastian.westenhoff.2@gu.se, e-stojkovic@neiu.edu; smarius@uwm.edu*

26

27

28

29 **Abstract**

30 Phytochromes are red/far-red light photoreceptors in bacteria to plants, which elicit a variety of
31 important physiological responses. They display a reversible photocycle between the resting (dark)
32 Pr state and the light activated Pfr state, in which light signals are received and transduced as
33 structural change through the entire protein to modulate the activity of the protein. It is unknown
34 how the Pr-to-Pfr interconversion occurs as the structure of intermediates remain notoriously
35 elusive. Here, we present short-lived crystal structures of the classical phytochrome from
36 myxobacterium *Stigmatella aurantiaca* captured by an X-ray Free Electron Laser 5 ns and 33ms
37 after light illumination of the Pr state. We observe large structural displacements of the covalently
38 bound bilin chromophore, which trigger a bifurcated signaling pathway. The snapshots show with
39 atomic precision how the signal progresses from the chromophore towards the output domains,
40 explaining how plants, bacteria and fungi sense red light.

41

42 **Keywords**

43 Bacteriophytochrome, Photocycle, Pr, Pfr, Lumi-R, X-ray Free Electron Lasers, Photoconversion,
44 Infrared Fluorescent Protein (IFP) Tissue Markers, PCM-Photosensory Core Module, Time-
45 resolved serial femtosecond crystallography

46

47

48

49

50

51

52

53 Introduction

54 Phytochromes are red-light protein photoreceptors, initially discovered in plants¹ where
55 they regulate essential physiological responses such as shade avoidance and etiolation². With that
56 they are critical to the thriving of all vegetation on earth. Homologous proteins exist in bacteria^{3,4},
57 cyanobacteria^{5,6} and fungi⁷. In photosynthetic bacteria, they regulate the synthesis of light-
58 harvesting complexes⁸⁻¹². In non-photosynthetic bacteria their role is less understood, but they are
59 involved in various processes such as the regulation of carotenoid pigments, which protect from
60 harmful light exposure⁴, in conjugation¹³, plant colonization¹⁴, quorum sensing and multicellular
61 fruiting body formation^{15,16}. Bacteriophytochromes (BphP) have also been successfully used as
62 infrared fluorescent tissue markers in mammals¹⁷.

63 Phytochromes consist of 2 modules, where the N-terminal photosensory core module
64 (PCM) is attached to a C-terminal effector module¹⁸. The latter module provides enzymatic activity
65 together with a so-called N-terminal extension¹⁹. In plant and class I BphPs the PCM consists of
66 three domains called PAS (Per-ARNT-Sim), GAF (cGMP phosphodiesterase/ adenylate
67 cyclase/FhlA), and PHY (phytochrome-specific) (Fig. 1 a, b). The module is conserved from
68 bacteria to plants and holds a covalently bound bilin chromophore, an open chain tetrapyrrole,
69 which is biliverdin IX α (BV) in bacteria (Fig. 2 b). Hallmark features are a conserved water
70 molecule in the center of the biliverdin, called the pyrrole water (PW)²⁰, the so-called PHY
71 (sensory) tongue, which changes fold in the Pr-to-Pfr transition²¹, and the long helix along the
72 dimer interface, which spans the entire PAS/GAF and PHY domains^{22,23}. The C-terminal effector
73 domain is divergent between species and is often a histidine kinase in bacteriophytochromes^{18,24,25}
74 Full length phytochromes are difficult to crystallize, but the PCM forms crystals that diffract to 2
75 Å resolution and beyond²⁶. They are particularly suited for time-resolved crystallographic
76 investigations.

77 Phytochromes display a photocycle (Fig. 2 a) with two half-cycles that are driven by two
78 different wavelengths of light. In classical phytochromes, the dark-adapted state, denoted as Pr,
79 absorbs red light ($\lambda \sim 700$ nm), which causes a *Z* to *E* isomerization of the C15=C16 double bond
80 within its bilin chromophore. Subsequent conformational changes of the entire protein end in a
81 far-red light absorbing state, denoted as Pfr. The Pfr state either relaxes thermally back to Pr, or

82 can be driven back to Pr by far-red light ($\lambda \sim 750$ nm). The structural changes associated with the
83 Pr to Pfr transition modulate the enzymatic activity of the phytochrome^{27,28}. Although the Pr and
84 Pfr states have been structurally characterized in detail using the *Deinococcus radiodurans*
85 (*Dr*)BphP PCM^{21-23,29}, structures of the nanosecond intermediates Lumi-R and Lumi-F as well as
86 those of the longer-lived intermediates in each photo-halfcycle (Fig. 2 a) are missing. In the Lumi-
87 R intermediate, the BV chromophore is in the electronic ground state. The 15Z anti (Fig. 2 b) to
88 15E anti isomerization of the C15=C16 double bond between rings C and D of the BV
89 chromophore should have taken place, resulting in a nearly 180° rotation of the D-ring³⁰⁻³². (Fig.
90 2 a).

91 Through the latest developments in time-resolved serial x-ray crystallography (TR-SFX),
92 the 1 ps structure of the truncated *Dr*BphP chromophore binding domain (CBD) that consists only
93 of the PAS and GAF domains was determined³³. 1ps after photoexcitation the BV D-ring in the
94 *Dr*BphP CBD rotates counter-clockwise, while the PW becomes photodissociated from the
95 chromophore binding pocket. Displacements of important, conserved amino acid residues are
96 observed already at 1 ps. For example, the conserved Asp-207 in the GAF domain moves
97 significantly, which could imply signaling directed towards the PHY-sensory tongue. However,
98 the PHY domain is not present in the CBD construct. Experiments on the entire PCM including
99 the critical PHY domain and sensory tongue are necessary to understand how the light signal is
100 transduced to the C-terminal enzymatic domain.

101 Previous attempts to initiate the photocycle in PCM crystals of various BphPs at room
102 temperature were unsuccessful presumably because the PCM constructs were not photoactive in
103 the crystal form, the illumination protocol was sub-optimal and/or the spatial resolution reached at
104 room temperature was not sufficient^{16,34}. Recently, we published the structure of a classical
105 phytochrome from non-photosynthetic myxobacterium *S. aurantiaca*, denoted *Sa*BphP2 PCM
106 solved to a resolution of 1.65 Å at cryogenic temperatures (100 K) in the Pr form. *Sa*BphP2 PCM
107 microcrystals are photoactive (Fig. 2 c) and diffract to 2.1 Å resolution at room temperature²⁶
108 which provides an opportunity to describe the Pr to Pfr transition by TR-SFX experiments.

109 The TR-SFX experiments on the *Sa*BphP2 PCM reported here were conducted at the
110 Japanese XFEL, the Spring-8 Angstrom Compact X-ray Laser (SACLA). They resulted in room

111 temperature structures 5 ns and 33 ms after light illumination of the Pr (dark) state with 640 nm
112 laser pulses (Methods and Extended Data Tab. 1). Results are discussed in terms of extensive
113 rearrangements of BV, specifically the D-ring, the PW and neighboring water network and
114 conserved amino acids in the GAF and PHY domains.

115 **Results**

116 **Difference Electron Density at 5ns and 33 ms.**

117 The difference electron density (DED) maps calculated at the 5 ns and 33 ms time delays
118 shows a large number of correlated positive and negative DED features in the PAS-GAF as well
119 as in the PHY domains (Fig. 3, Extended Data Tab. 2, see Methods and Extended Data Table 3 for
120 a statistical assessment). These features indicate structural changes through the entire *SaBphP2*
121 PCM dimer. The control map at 66 ms only contains spurious features, supporting this assignment
122 (Fig. 3). In all previous ns time-resolved crystallographic experiments on photoactive yellow
123 protein^{35,36}, myoglobin^{37,38}, and others^{39,40} DED features are mostly localized to the chromophore
124 and a few residues. As a consequence, the DED map sigma level is determined by the noise in the
125 DED map as has been shown previously⁴¹. Here, this is different. The map sigma level is
126 determined by both the noise and the signal. The large number of difference features poses a
127 formidable challenge for the interpretation of the DED maps, as well as for structure determination.
128 The features must be interpreted locally near the chromophore and the chromophore pocket, and
129 more globally for the entire *SaBphP2* PCM dimer (see Methods). Standard deviations (σ) of the
130 DED maps are determined by both the noise and the signal. We therefore use the σ values of the
131 66 ms control DED map to contour the 5ns and 33ms maps and to identify chemically meaningful
132 signals.

133 **Ring-D Orientations at 5ns and 33ms**

134 Substantial DED features are observed on and near the BV chromophore (Fig. 3, 5 ns insert
135 and Fig. 4). Strong negative DED features on the D-ring carbonyl, methyl and vinyl mark
136 substantial structural rearrangements in both subunits. Interestingly, positive features that identify
137 D-ring orientations upon light illumination differ in subunit A and in B. In subunit A, there are
138 strong lateral features (β_1 to β_4) that support a clockwise $\sim 90^\circ$ twist of the D-ring (Extended Data
139 Fig. 1 b-e) when viewed along the chromophore axis from the D to the A-ring. These features can
140 be reproduced by calculated difference maps (compare Extended Data Fig. 1 b,c and d,e). In

141 addition, positive features ξ (Fig. 4 a) are oriented in a way that support a 180° rotation. For the
142 interpretation of features ξ , extrapolated electron density (EED) maps were necessary since the
143 strong negative density on the D-ring carbonyl tends to eliminate close-by positive features. Ring-
144 like electron density appears in the EED maps (Fig. 4 b) indicating a fully isomerized D-ring.
145 Accordingly, two conformations of the chromophore are need to interpret the positive DED to
146 completion, a $\sim 90^\circ$ clockwise D-ring twist and a fully isomerized $\sim 180^\circ$ clockwise D-ring rotation
147 (Fig. 4 b, Extended Data Tab. 4).

148 In subunit B, features ξ are absent (Fig. 4 c). In accordance, EED maps (Fig. 4 d) do not
149 support a fully isomerized configuration (as in subunit A) for both the 5 ns and the 33 ms time
150 delays. Instead, strong positive features determine the geometry of the BV A to C-rings; see Fig.
151 4 a and c for a comparison of the DED in both subunits. In subunit B the entire BV pivots about
152 the B-ring (Fig. 4 c) which leads to strong C-ring and D-ring displacements. To interpret positive
153 features β_{c1} and β_{c2} ('c' for clockwise) C-ring must be tilted backwards (blue arrow in Fig. 4 c)
154 and the ring-D can only be oriented clockwise (light blue BV structure in Fig. 4 c,d) to fit the DED.
155 This leaves a strong feature β_{a1} which is located behind the C-ring plane. To reproduce this feature,
156 the ring C propionyl must tilt in the opposite direction (purple arrow in Fig. 4 c) which leads to a
157 displacement of carbon atom C_{15} forward. Then, the counter-clockwise D-ring orientation (in pink)
158 fits the DED.

159 **Amino acid and water network rearrangement in the chromophore binding pocket and the** 160 **sensory tongue**

161 Strong negative DED features indicate that the PW photo-dissociated from BV in both
162 subunits at 5ns and 33ms (Fig. 4, Extended Data Tab. 2). Moreover, significant displacements of
163 the conserved Asp-192 of the PASDIP consensus sequence in the GAF domain and the Arg-457
164 of the PRXSF motif^{22,42} in the PHY domain are observed in subunit A (and at 33 ms also in subunit
165 B). Asp-192 and Arg-457 form a salt bridge, anchoring the PHY tongue to the chromophore region
166 in the Pr state. This connection is broken at 5ns. A strong positive DED feature between these two
167 amino acids is observed, indicating a water molecule (Fig. 5 a). Furthermore, the conserved Tyr-
168 248 in proximity to Asp-192 adopts a dual conformation at 5 ns and 33 ms (Extended Data Fig.
169 2). Similarly, a dual conformation is observed for the conserved His-275 (at 33 ms) that forms a
170 hydrogen bond to the D-ring carbonyl in the Pr state of the *Sa*BphP2 and other classical BphPs. In

171 contrast to these amino acid rearrangements, the structure of the sensory tongue is only locally
172 affected (Fig. 5 c). A β -sheet to α -helix transition is not observed which coincides with only minor
173 changes of the PHY domain position (Fig. 5 d,e).

174 On the other side of the chromophore, opposite to the tongue region, strong features in the
175 DED maps at 5ns and 33 ms indicate that the BV C-ring propionyl drags the conserved Ser-257
176 and Ser-259 along at 5ns and 33 ms. (Fig. 5 b, see also Extended Data Tabs. 2 and 4). A positive
177 DED feature in the B subunit indicates the appearance of a water molecule that may form hydrogen
178 bonds with the C-ring propionyl as well as with Ser-257 and Ser-259. Moreover, the DED maps
179 show correlated negative and positive features within the PAS-GAF domains and along the long
180 helices that form the dimer interface (Fig 3), pushing outwards the C-terminal helix that connects
181 to the output module (Fig 5 d and e). We propose that the structural changes in the chromophore
182 pocket initiate the signal that is transduced along the long helices ‘wiring’ together the BV
183 chromophore and effector domains.

184 Discussion

185 Global and local structural relaxations at 5 ns and 33 ms post illumination

186 In the *DrBphP* CBD protein relaxations can already observed at 1 ps and 10 ps³³. Although
187 individual BV ring displacements are observed, the chromophore essentially stays at the position
188 that it also occupies in the dark structure (Extended Data Tab. 5). Despite this, the signal has
189 penetrated deep into the BV-pocket of the GAF domain³³. On the ns time-scale the signal is
190 expanding further through the entire PCM of the classical *SaBphP2*. In contrast to smaller proteins,
191 such as PYP and myoglobin, the *SaBphP2* is large and flexible and can react readily and fast to
192 local chromophore perturbations. In the *SaBphP2* PCM structures shown here, protein relaxations
193 are advanced enough that large chromophore displacements are observed in both subunits.
194 Especially in subunit B, large chromophore geometry distortions are present (Extended Data Tab.
195 4) as the C-ring tilts out in both directions. It appears as if the energy of the absorbed photon is
196 stored in a distorted BV geometry that drives protein relaxations. Chromophore geometry
197 distortions are also found in early intermediates of unrelated proteins such as the PYP³⁵.
198 Distortions of the BV chromophore of the phytochrome photocycle have been also predicted by
199 time-resolved spectroscopy³¹. They were directly observed in temperature scan cryo-
200 crystallography experiments performed on the bathy phytochrome *PaBphP* from *Pseudomonas*

201 *aeruginosa*⁴³ (Extended Data Tab. 5) further suggesting that distorted chromophore conformations
202 are part of an important mechanism to advance photochemical reactions. As the BV chromophore
203 position changes, it strongly affects amino acid residues near the BV propionyl moieties that shift
204 in unison with the chromophore. Examples are listed in Extended Data Tab. 2 and 4, and are
205 discussed further down. The species with the full 180° rotation of the D-ring might be associated
206 with a key Lumi-R like intermediate in the phytochrome photocycle (Fig. 2 a). To determine the
207 specific time point where the 180° rotation begins, additional data collected at different time delays
208 are required.

209 The absence of the fully isomerized D-ring isoform in subunit B can likely be explained
210 by differences in the subunits related by non-crystallographic symmetry. As the structure of the
211 sensory tongue is essentially identical in both subunits, it is unlikely the reason for this behavior.
212 By inspecting the region near Cys-13 to which the BV chromophore is bound, differences are
213 found. Distances to symmetry related molecules are different for subunit A and B. In subunit A
214 the distances from Arg-15 to Gln-139 and Cys-13 (S) to Lys-136 (N_Z) (Gln-139 and Lys-136
215 belong to the molecule related by crystallographic symmetry) are 6.0 Å and 7.2 Å, respectively.
216 These distances are smaller in subunit B (5.2 Å, and 4.0 Å, respectively). These differences likely
217 have an impact on chromophore relaxations, as in subunit B BV structure appears more distorted
218 than in subunit A (see twisting angles for subunits A and B in Extended Data Tab. 4).

219 **Rearrangement of water network and neighboring amino acids**

220 The PW forms a stable hydrogen bond network with BV rings A-C in both the Pr and Pfr
221 states, but it is absent at 5 ns and 33 ms. It photo-dissociates already within 1 ps in the *DrBphP*
222 CBD fragmentation³³. While the twisting motion of D-ring has been the working model for
223 phytochrome activation and now has been confirmed, the disappearance of the PW is surprising.
224 Given the large sliding motions of the chromophore (Fig. 4 a and c), this now makes sense as the
225 absence of the PW most likely enables these displacements. It is interesting to note that the PW
226 dissociates very early³³ and rebinds back to BV in Pfr^{21,29}. The PW may have a dual role in
227 facilitating the structural transition and stabilizing the reaction product (Pr as well as Pfr) in both
228 halves of the reaction cycle. Both, the rotation of the D-ring together with photodissociation of the
229 PW likely are the main triggers for subsequent protein structural changes. Together, they transduce

230 the light signal to the sensory tongue of the PHY domain and cause relaxations of the GAF domain
231 that propagate further up the long helices along the dimer interface.

232 **Sensory tongue and the PHY domain**

233 The sensory tongue connects the PHY domain directly with the chromophore region (Fig.
234 5). During the full Pr to Pfr transition the sensory tongue undergoes extensive structural
235 transitions from a beta sheet to an alpha helix^{21,29}. In the Pfr state, Pro-456 becomes adjacent to
236 the D-ring and forms a hydrogen bond with Tyr-248. This is stabilizing the D-ring in E
237 configuration. It is interesting to ask how this shift is initiated. In the present microcrystals, the
238 transition is not observed (Fig. 5 c). We ascribe this to the crowded environment of the crystals.
239 However, the tight Asp-192 to Arg-457 salt bridge is already broken at 5 ns and a water is inserted
240 in between the residues. This is an important first step to enable the sensory tongue to rearrange.
241 We therefore conclude that the signal is transduced to the PHY tongue via the displacement of the
242 chromophore that enforces the movement of Asp-129 and the photo-dissociation of the PW.

243 **Propagation of the light signal**

244 Caused by D-ring rotation, the conserved Tyr-248 moves (Extended Data Fig. 2). This
245 destabilizes interactions with the neighboring amino acids and the water network. Arg-457 and
246 Asp-192 form new hydrogen bonds with a water molecule (Fig. 5 a). As the chromophore slides
247 substantially (Fig. 4), it induces structural changes in the GAF domain sensed by the conserved
248 serines 257, 259 and 261 and multiple other amino acids near the chromophore. His-275 loses
249 contact with the ring-D carbonyl (distance: $> 4 \text{ \AA}$) and with the more distant Arg-157 (now ~ 4.0
250 \AA) that lead to substantial GAF domain relaxations which are ultimately relayed to the PHY
251 domain through the long dimer-interface helices. As the speed of sound in protein crystals is about
252 2000 m/s^{44} , heat expansion through 100 \AA of protein (roughly the length of the *SaBphP2* PCM) in
253 5 ns cannot be excluded. However, relaxations at 33 ns are very similar to those at 5 ns. Heat
254 produced locally after chromophore light absorption should have dissipated by then, and the DED
255 features at 5 ns rather represent genuine protein relaxations.

256 The changes on the long dimer helix and the C-terminal helix (Fig. 3) suggest a mechanism
257 of signal transduction that does not rely exclusively on the opening of the PHY domains (Fig. 1
258 b). It seems as the long helices, and not so much the sensory tongues, translate the signal towards

259 the small C-terminal helices that are connected to the coiled-coil linker region of the effector
260 domain (Fig. 5 d,e, red arrows). This confirms a suggestion that was made based on the static
261 crystal structures of the bathy *PaBphP* PCM²³ and compares favorably to signal transduction in
262 transmembrane sensory proteins⁴⁵. Only small PHY domain displacements (Fig. 5 d,e) are
263 necessary for signal transduction. Since the linker helices of the sister monomers are at an angle,
264 translations along their axes will slightly change the relative orientation of the effector domains,
265 and hence their activity, possibly modulated by a shift in register of the coiled coil linker²⁷.

266 **Summary and outlook**

267 The short-lived structural intermediates presented here establish that it is indeed the
268 isomerization of the D-ring, which drives the photoconversion in phytochromes. The remaining
269 rings of the chromophore move notable distances and the movements are heterogeneous between
270 the different subunits. The presence of unproductive BV conformations, may explain the relatively
271 low quantum yield for the Pr to Pfr transition (approximately 10-15%). Nevertheless, we observe
272 a fully isomerized BV configuration and establish that photodissociation of the PW and the
273 displacements of the strictly conserved Asp-195 and Tyr 248 lead to a disconnection of the PHY
274 sensory tongue from the chromophore region. Finally, the data show strong evidence for a
275 structural change along the long helices at the dimer interfaces that transduce the signal further
276 towards the PHY domains.

277 Earlier time points within the *SaBphP2*-WT PCM photocycle should be collected to assess
278 when the large BV chromophore displacements begin. Large scale structural changes are limited
279 by the crystal packing. Therefore, methods, which act on proteins in solution should be explored
280 to make further progress. Recently, solution NMR spectra of a full PCM was assigned for a
281 phytochrome⁴⁶ and new developments in cryoEM⁴⁷ bring atomic resolution of macromolecular
282 structures within reach without the need for crystals. Calculations are underway⁴⁸ explaining how
283 to obtain structures from single biological macromolecules, such as the full-length, intact BphPs
284 at XFELs.

285 **Methods**

286 **Protein purification and crystallization**

287 Microcrystals of the *SaBphP2*-PCM were grown as described⁴⁹ by mixing a mother liquor
288 consisting of 0.17 M Ammonium acetate, 0.085 M Sodium citrate tribasic dihydrate pH 5.6, 25.5%
289 w/v Polyethylene glycol 4000, 15% v/v Glycerol (cryo-screen solution) and 3 % w/v Benzamidine
290 Hydrochloride, with 60 mg/mL protein (3:2 protein to mother liquor ratio). The mixture was
291 seeded with finely crushed macrocrystals. After 4 days, the microcrystals were collected and
292 concentrated to about 10¹¹ crystals /ml and subsequently folded into a tenfold amount of nuclear
293 grade grease^{50,51}. All steps in crystallization and tray observations were performed under green
294 safety light.

295 **Experimental Setup.**

296 Pump-probe experiments were conducted at beamline BL2 at SACLA using a nanosecond
297 laser^{52,53}. For our nanosecond TR-SFX experiments a two-sided laser illumination geometry was
298 used where a split laser beam intercepts the X-rays and the viscous jet at a 90° angle from opposite
299 sides. A relatively large laser fluence of 3.5 mJ/mm² was chosen for each side, respectively. The
300 laser fluence was chosen based on absorption measurements on grease crystal mixtures (Extended
301 Data Fig. 3, see also below). For femtosecond TR-SFX experiments X-rays and laser illumination
302 are parallel^{33,39,54-57}. Then, the effective ‘hit-rate’ of the laser illumination is equivalent to the X-
303 ray hit-rate^{54,55} and shading by other crystals in the viscous jet does not play a role. This has
304 consequences for the selection of the laser fluence, especially for fs laser illumination, which are
305 discussed^{54,55}. In contrast, for a perpendicular geometry as employed here, the entire path of the
306 X-ray beam through the crystal must be illuminated by the laser. This leads to an effective laser
307 beam size that is much larger than the X-ray beam (Extended Data Fig. 3 b). The large effective
308 laser beam size is likely intercepted by other crystals in the relatively thick (100 μm) viscous jet.
309 This results in substantial shading by crystals not exposed to the X-rays. To roughly estimate this
310 shading, the crystal-grease mixtures were sandwiched between cover slides kept apart by 50 μm
311 washers to match the optical path through half of the 100 μm thick viscous jet. Absorption was
312 measured with a microspectrophotometer located at BioCARS (APS, Argonne National
313 Laboratory). Grease mixed with *SaBphP2* PCM microcrystals shows an absorption of 0.75 at 640
314 nm (Extended Data Fig. 3 a), which corresponds to a 5 fold reduction of the incident fluence. In
315 addition, at 640 nm the absorption is only 40% of that at the maximum at 700 nm. Accordingly, a
316 3.5 mJ/mm² fluence at 640 nm is equivalent to only about 0.28 mJ/mm² at the absorption
317 maximum. Because of the 2-sided illumination the total fluence at a crystal probed in the middle

318 of the jet is 0.56 mJ/mm^2 (with reference to the absorption maximum). Given the previous
319 experiences with photoactive yellow protein^{36,56}, 0.56 mJ/mm^2 is well below the threshold to
320 generate damage even with femtosecond laser pulses⁵⁸, and does not play any adverse role with
321 nanosecond laser pulses. We believe that for our experimental geometry strong laser excitation has
322 been essential to boost excitation levels to the extent that analyzable signal is obtained.

323 **TR-SFX data acquisition and processing**

324 200 μl of the crystal-grease mixture were transferred into an injector reservoir⁵⁹ and
325 extruded into air at ambient temperatures (293 K) through a 100 μm wide nozzle with a flow rate
326 of about 4 $\mu\text{l}/\text{min}$. The photoreaction was started with 5 ns lasers pulses of 640 nm wavelength
327 with a full width half maximum (FWHM) of 52 μm . The laser repetition rate was varied between
328 15 Hz and 10 Hz (Extended Data Fig. 4). A flow rate of 4 $\mu\text{l}/\text{min}$ displaces at least a 300 μm
329 column of grease between the high frequency (15 Hz) laser pulses. 5 ns after the laser pulse the
330 stream of microcrystals was exposed in air to intense X-ray pulses ($\lambda = 1.38 \text{ \AA}$) of $< 10 \text{ fs}$ duration
331 with either 10 Hz or 15 Hz repetition rates. The scattering background was minimized by using a
332 helium-purged collimator. We used a pump-probe, 33 ms, 66 ms (Extended Data Fig. 4 b) data
333 collection strategy to assess whether a once laser illuminated/excited viscous jet volume has left
334 the X-ray interaction region and moved sufficiently that multiple laser excitations of the X-ray
335 probed volume are avoided.

336 Reference data which are free of laser excitation have been collected previously without
337 the laser²⁶. For all experiments, diffraction patterns were collected on a CCD detector with eight
338 modules⁶⁰ and analyzed with a user-friendly data-processing pipeline⁶¹ consisting of hit-finding
339 with Cheetah⁶², and indexing and Monte Carlo integration by CrystFEL⁶³. The hit rate was about
340 30%. About 50 % of diffraction patterns were successfully indexed. Mosflm and DirAx both were
341 used for indexing. The extracted partial intensities were merged to full reflection intensities using
342 the ‘partialator’ program in CrystFEL. For data statistics, see Extended Data Tab. 1. The full
343 intensities were converted to structure-factor amplitudes by software based on the CCP4 suite of
344 programs⁶⁴.

345 **Computation of Difference Electron Density Maps**

346 Weighted difference electron density (DED) maps were calculated as described^{36,65}. The
347 DED maps at 33 ms and 66 ms were inspected for strong DED features near the chromophore. At

348 33 ms clear signal is present (Extended Data Fig. 5 b). At 66 ms, only spurious and randomly
349 distributed features could be detected (Extended Data Fig. 5 c). This demonstrates that the viscous
350 jet is extruded fast enough to cope with a data collection strategy shown in Extended Data Fig. 4
351 a (pump-probe, dark) as with this strategy the next laser pulses arrives 66 ms after the previous
352 one. This way, the laser excites a pristine jet volume that is free from contaminations from earlier
353 laser pulses. Data for two time-delays are collected from the same experimental setup, as the first
354 X-ray pulse after laser excitation contributes diffraction patterns for a 5 ns dataset, the second X-
355 ray pulse contributes to a 33 ms dataset. Needless to say, when only one intermittent X-ray pulse
356 is used (Extended Data Fig. 4 a, the reference data must be collected separately with the laser
357 switched off (see above).

358 **Statistical Analysis of DED Features**

359 The signal content and signal variance (sigma values) in the DED maps were analyzed by
360 histograms. Gaussian fits to the histogram should reproduce the root mean square deviation
361 (RMSD) values of the fft program that calculates the DED when the signal is purely random. When
362 the signal is weak and localized, it only changes the distribution in the flanks of the Gaussian⁶⁶,
363 but not the sigma value. If the signal is strong and everywhere, the fitted Gaussian becomes broader
364 and does not fit the flanks. The noise originates from the experimental error in the difference
365 amplitudes and errors introduced by the Fourier approximation⁶⁷. In the presence of localized
366 signal, the noise and not the signal determines the sigma value of a DED map⁶⁶. Here, this is not
367 the case, and occurs for the first time in time-resolved crystallography. In Extended Data Fig. 6 b,
368 a histogram of DED values derived from difference amplitudes $\Delta F = F_{66\text{ms}} - F_{\text{Dark}}$ is shown. The
369 histogram is fit by a Gaussian with a sigma of $0.0125 \text{ e}^-/\text{\AA}^3$. The same value also reported by the
370 fast Fourier program ('fft') from the ccp4 suite of programs. The Gaussian fits the histogram
371 perfectly which outlines the random nature of the DED features. A histogram prepared from the
372 $5\text{ns} - F_{\text{dark}}$ DED_{5ns} map is shown in Extended Data Fig. 6 a. The Gaussian is broader as in Extended
373 Data Fig. 6 b, and the flanks of the histogram are not fit properly by the Gaussian. If the DED
374 features containing signal would be sparse, the sigma from the fit would be essentially identical to
375 the value obtained from the 66 ms control data only. However, it is larger, $0.0144 \text{ e}^-/\text{\AA}^3$. The form
376 of the histogram is an indication of strong signal throughout the map. For the DED_{5ns} map the
377 sigma value is determined by all of the noise sources described above plus the signal.
378 Consequently, for meaningful comparisons, the DED_{5ns} map must be contoured as a multiple of

379 the sigma value found in the DED_{66ms} control map, as this reflects the error level in a DED map
380 without signal.

381 As large numbers of DED features were found, it is useful to estimate how many of these
382 features might be generated by the noise sources mentioned above. For this, DED maps were
383 sampled on a 3D grid no larger than $2(h_{\max} + 1)$ with h_{\max} the maximum h,k and l values within the
384 resolution limit. As an example: at a resolution of 2 Å and a unit cell axis $a = 80$ Å, h_{\max} is 40.
385 Assuming similar values for the other cell axes, the unit cell and its DED content is sampled on a
386 82 x 82 x 82 grid. This way the DED peaks found in such a map correspond to independent
387 features. Extended Data Tab. 3 contrasts the number of DED features observed at 33 ms to the
388 ones expected to occur randomly in the DED map. On the 3 sigma level, for example, 1839 features
389 are expected to be purely random, and 3167 features are observed. On the 5 sigma level, the
390 probability of a feature to be random is so low that not even one feature is expected in the entire
391 DED map, yet 264 features (132 for a *SaBphP2* PCM dimer located in the asymmetric unit) are
392 observed. To bring this into perspective, in the strong difference map determined for the
393 photoactive yellow protein at a 3 ps pump-probe time delay⁵⁶, only 12 features, two per symmetry
394 related PYP molecule, are observed on the 5 sigma level (at 2.1 Å resolution to be compatible with
395 the resolution achieved here, and h_{\max} determined as described).

396 **Structure determination**

397 Structural models were derived from extrapolated maps calculated by adding $N \cdot DF$ to the
398 structure factors calculated from an accurately refined dark state *SaBphP2* PCM model. The factor
399 N_C required to extrapolate the fraction of excited molecules to 100 % was determined by
400 integrating negative density in the extrapolated maps until the values diverge (Extended Data Fig.
401 7). For the 5 ns time delay N_C is 19 which corresponds to a population of 10.5 % activated
402 molecules in the crystal⁶⁵. For the 33 ms time delay N_C is 22 (about 9% of molecules are activated).
403 The chromophore was moved by hand into the extrapolated maps calculated at 5 ns and 33 ms
404 time delays. The D-ring was rotated about the double bond $\Delta 15,16$ to achieve maximum agreement
405 with the DED maps as well as with the extrapolated density. Multiple D-ring orientations were
406 accommodated by generating chromophore double conformations. The apo-*SaBphP2* PCM
407 structures were determined by using the real space (stepped) refinement option in 'coot'. This was
408 followed by a scripted 'zoned' refinement, also performed in real space in 'coot'. For this, the

409 script activates α -helical and β -strain restraints when needed. After the real space refinement the
410 agreement with the difference map was inspected, and if necessary corrected further by hand.
411 Double conformations for certain residues (His275, Tyr 248) were introduced to accommodate
412 DED features that result from the various D-ring orientations. If in doubt, extrapolated maps with
413 higher N ($N \sim 40$) were computed to verify the presence or to clarify the absence of individual
414 structural moieties at specific locations in space. A final reciprocal space refinement was
415 conducted using phased extrapolated structure factors (PESF) calculated as described
416 previously^{33,65,68}. As calculated structure factors of the reference structure are used to determine
417 the PESFs, the final refinement is biased towards the reference (dark) structure. Therefore, refined
418 differences are (i) real, and (ii) sometimes tend to be underdetermined by a fraction of an Å.
419 Extrapolated amplitudes also amplify errors in the difference amplitudes N_c times. Due to this,
420 structures were refined to 2.4 Å which is lower than the resolution limit of the data. Due to the
421 same reasons, occupancies for the chromophore and other amino acid residues double
422 conformations were not refined. Occupancies were rather distributed on equal par among the
423 double conformations.

424 **Pearson Correlation Coefficient to estimate ring-D orientation.**

425 Once a model that interprets the DED is determined, calculated DED maps can be
426 computed from this model and the reference model^{33,68} by subtracting structure factors calculated
427 from both models. In order to corroborate the assessment of clockwise and counter-clockwise D-
428 ring rotation, the Pearson Correlation Coefficient was used. For the correlation coefficient the
429 observed and calculated DED maps are compared. Since negative DED is always on top of the
430 reference model, the negative DED does not add information to distinguish competing models.
431 Accordingly, only positive DED features near the ring-D region are compared. A Fortran program
432 was developed that reads difference maps in ccp4 format, masks out a specific volume around a
433 pdb-file provided to the program, and calculates the Pearson correlation coefficient (PCC) within
434 this masked volume. Here, the mask volume is determined by the coordinates of the D-ring in both
435 clockwise and counter-clockwise orientations. Within this volume, the PCC was determined by a
436 grid-wise comparison of positive observed and corresponding calculated DED features as:

437

438

$$PCC = \frac{\sum_i (\Delta\rho^{obs} - \langle \Delta\rho^{obs} \rangle) (\Delta\rho^{calc} - \langle \Delta\rho^{calc} \rangle)}{\sqrt{\sum_i (\Delta\rho^{obs} - \langle \Delta\rho^{obs} \rangle)^2} \sqrt{\sum_i (\Delta\rho^{calc} - \langle \Delta\rho^{calc} \rangle)^2}}.$$

439

440 The terms in the bracket are the averages computed from all grid points i in the mask. Although
441 the average DED in an entire difference map is zero, the averages computed here are not zero,
442 since only positive features are evaluated. In addition, map grid points i were selected only when
443 the observed DED values are larger than a certain sigma value. With this, the PCC can be plotted
444 as a function of increasing sigma values (see Extended Data Fig. 8). In subunit A, at 5 ns, only the
445 clockwise rotation is supported in particular by high DED features. In subunit B, the PCC is similar
446 regardless whether a model with a clockwise, a counter-clockwise or a double conformation is
447 examined. This demonstrates that both clockwise and counter-clockwise ring-D rotations produce
448 calculated DED features that explain the observed density equally well. The PCC cannot
449 distinguish between the two ring-D orientations.

450 **Detailed Views of Structural Moieties.**

451 Structural views were generated by UCSF Chimera⁶⁹.

452

453

454 **References**

- 455 1 Butler, W. L., Norris, K. H., Siegelman, H. W. & Hendricks, S. B. Detection, assay, and
456 preliminary purification of the pigment controlling photoresponsive development of plants.
457 *Proceedings of the National Academy of Sciences of the United States of America* **89**, 6 (1959).
- 458 2 Batschauer, A. Photoreceptors of higher plants. *Planta* **206**, 479-492, doi:DOI
459 10.1007/s004250050425 (1998).
- 460 3 Jiang, Z. *et al.* Bacterial photoreceptor with similarity to photoactive yellow protein and plant
461 phytochromes. *Science* **285**, 406-409 (1999).
- 462 4 Davis, S. J., Vener, A. V. & Vierstra, R. D. Bacteriophytochromes: Phytochrome-like
463 photoreceptors from nonphotosynthetic eubacteria. *Science* **286**, 2517-2520, doi:DOI
464 10.1126/science.286.5449.2517 (1999).
- 465 5 Hughes, J. *et al.* A prokaryotic phytochrome. *Nature* **386**, 663, doi:10.1038/386663a0 (1997).
- 466 6 Yeh, K. C., Wu, S. H., Murphy, J. T. & Lagarias, J. C. A cyanobacterial phytochrome two-
467 component light sensory system. *Science* **277**, 1505-1508, doi:10.1126/science.277.5331.1505
468 (1997).
- 469 7 Blumenstein, A. *et al.* The *Aspergillus nidulans* phytochrome FphA represses sexual development
470 in red light. *Curr Biol* **15**, 1833-1838, doi:10.1016/j.cub.2005.08.061 (2005).
- 471 8 Yang, X. *et al.* Light Signaling Mechanism of Two Tandem Bacteriophytochromes. *Structure* **23**,
472 1179-1189, doi:10.1016/j.str.2015.04.022 (2015).
- 473 9 Toh, K. C., Stojkovic, E. A., van Stokkum, I. H. M., Moffat, K. & Kennis, J. T. The
474 Photochemistry of Bacteriophytochrome: Key to its Use as a Deep-Tissue Fluorescence Probe.
475 *Biophysical journal* **100**, 174-174 (2011).
- 476 10 Giraud, E. *et al.* Bacteriophytochrome controls photosystem synthesis in anoxygenic bacteria.
477 *Nature* **417**, 202-205, doi:10.1038/417202a (2002).
- 478 11 Fixen, K. R., Baker, A. W., Stojkovic, E. A., Beatty, J. T. & Harwood, C. S. Apo-
479 bacteriophytochromes modulate bacterial photosynthesis in response to low light. *Proceedings of*
480 *the National Academy of Sciences of the United States of America* **111**, E237-244,
481 doi:10.1073/pnas.1322410111 (2014).
- 482 12 Yang, X., Stojkovic, E. A., Kuk, J. & Moffat, K. Crystal structure of the chromophore binding
483 domain of an unusual bacteriophytochrome, RpBphP3, reveals residues that modulate
484 photoconversion. *Proceedings of the National Academy of Sciences of the United States of*
485 *America* **104**, 12571-12576, doi:10.1073/pnas.0701737104 (2007).
- 486 13 Bai, Y., Rottwinkel, G., Feng, J., Liu, Y. & Lamparter, T. Bacteriophytochromes control
487 conjugation in *Agrobacterium fabrum*. *Journal of photochemistry and photobiology. B, Biology*
488 **161**, 192-199, doi:10.1016/j.jphotobiol.2016.05.014 (2016).
- 489 14 McGrane, R. & Beattie, G. A. *Pseudomonas syringae* pv. *syringae* B728a Regulates Multiple
490 Stages of Plant Colonization via the Bacteriophytochrome BphP1. *MBio* **8**,
491 doi:10.1128/mBio.01178-17 (2017).

- 492 15 Barkovits, K., Schubert, B., Heine, S., Scheer, M. & Frankenberg-Dinkel, N. Function of the
493 bacteriophytochrome BphP in the RpoS/Las quorum-sensing network of *Pseudomonas*
494 *aeruginosa*. *Microbiology* **157**, 1651-1664, doi:10.1099/mic.0.049007-0 (2011).
- 495 16 Weitowich, N. C. *et al.* Structural basis for light control of cell development revealed by crystal
496 structures of a myxobacterial phytochrome. *IUCrJ* **5**, 619-634, doi:10.1107/S2052252518010631
497 (2018).
- 498 17 Shu, X. *et al.* Mammalian expression of infrared fluorescent proteins engineered from a bacterial
499 phytochrome. *Science* **324**, 804-807, doi:10.1126/science.1168683 (2009).
- 500 18 Auldridge, M. E. & Forest, K. T. Bacterial phytochromes: More than meets the light. *Crit Rev*
501 *Biochem Mol* **46**, 67-88, doi:Doi 10.3109/10409238.2010.546389 (2011).
- 502 19 Legris, M., Ince, Y. C. & Fankhauser, C. Molecular mechanisms underlying phytochrome-
503 controlled morphogenesis in plants. *Nat Commun* **10**, 5219, doi:10.1038/s41467-019-13045-0
504 (2019).
- 505 20 Wagner, J. R., Brunzelle, J. S., Forest, K. T. & Vierstra, R. D. A light-sensing knot revealed by
506 the structure of the chromophore-binding domain of phytochrome. *Nature* **438**, 325-331, doi:Doi
507 10.1038/Nature04118 (2005).
- 508 21 Takala, H. *et al.* Signal amplification and transduction in phytochrome photosensors. *Nature* **509**,
509 245-248, doi:10.1038/nature13310 (2014).
- 510 22 Essen, L. O., Mailliet, J. & Hughes, J. The structure of a complete phytochrome sensory module
511 in the Pr ground state. *Proceedings of the National Academy of Sciences of the United States of*
512 *America* **105**, 14709-14714, doi:10.1073/pnas.0806477105 (2008).
- 513 23 Yang, X., Kuk, J. & Moffat, K. Crystal structure of *Pseudomonas aeruginosa*
514 bacteriophytochrome: photoconversion and signal transduction. *Proceedings of the National*
515 *Academy of Sciences of the United States of America* **105**, 14715-14720,
516 doi:10.1073/pnas.0806718105 (2008).
- 517 24 Gourinchas, G. *et al.* Long-range allosteric signaling in red light-regulated diguanylyl cyclases.
518 *Sci Adv* **3**, e1602498, doi:10.1126/sciadv.1602498 (2017).
- 519 25 Otero, L. H. *et al.* Structure of the Full-Length Bacteriophytochrome from the Plant Pathogen
520 *Xanthomonas campestris* Provides Clues to its Long-Range Signaling Mechanism. *Journal of*
521 *molecular biology* **428**, 3702-3720, doi:10.1016/j.jmb.2016.04.012 (2016).
- 522 26 Sanchez, J. C. *et al.* High-resolution crystal structures of amyxobacterial phytochrome at cryo and
523 roomtemperatures. *Struct Dyn-Us* **6**, doi:10.1063/1.5120527 (2019).
- 524 27 Gourinchas, G., Heintz, U. & Winkler, A. Asymmetric activation mechanism of a homodimeric
525 red light-regulated photoreceptor. *eLife* **7**, doi:10.7554/eLife.34815 (2018).
- 526 28 Giraud, E. *et al.* A new type of bacteriophytochrome acts in tandem with a classical
527 bacteriophytochrome to control the antennae synthesis in *Rhodospseudomonas palustris*. *Journal*
528 *of Biological Chemistry* **280**, 32389-32397 (2005).

- 529 29 Burgie, E. S., Zhang, J. & Vierstra, R. D. Crystal Structure of Deinococcus Phytochrome in the
530 Photoactivated State Reveals a Cascade of Structural Rearrangements during Photoconversion.
531 *Structure* **24**, 448-457, doi:10.1016/j.str.2016.01.001 (2016).
- 532 30 Mathes, T. *et al.* Femto- to Microsecond Photodynamics of an Unusual Bacteriophytochrome. *J.*
533 *Phys. Chem. Lett.* **6**, 5, doi:10.1021/jz502408n (2014).
- 534 31 Toh, K. C., Stojkovic, E. A., van Stokkum, I. H., Moffat, K. & Kennis, J. T. Proton-transfer and
535 hydrogen-bond interactions determine fluorescence quantum yield and photochemical efficiency
536 of bacteriophytochrome. *Proceedings of the National Academy of Sciences of the United States of*
537 *America* **107**, 9170-9175, doi:10.1073/pnas.0911535107 (2010).
- 538 32 Schmidt, M., Patel, A., Zhao, Y. & Reuter, W. Structural basis for the photochemistry of alpha-
539 phycoerythrocyanin. *Biochemistry* **46**, 416-423, doi:10.1021/bi061844j (2007).
- 540 33 Claesson, E. *et al.* The primary structural photoresponse of phytochrome proteins captured by a
541 femtosecond X-ray laser. *eLife* **9**, doi:10.7554/eLife.53514 (2020).
- 542 34 Roessler, C. G. *et al.* Acoustic Injectors for Drop-On-Demand Serial Femtosecond
543 Crystallography. *Structure* **24**, 631-640, doi:10.1016/j.str.2016.02.007 (2016).
- 544 35 Jung, Y. O. *et al.* Volume-conserving trans-cis isomerization pathways in photoactive yellow
545 protein visualized by picosecond X-ray crystallography. *Nature chemistry* **5**, 212-220,
546 doi:10.1038/nchem.1565 (2013).
- 547 36 Tenboer, J. *et al.* Time-resolved serial crystallography captures high-resolution intermediates of
548 photoactive yellow protein. *Science* **346**, 1242-1246, doi:10.1126/science.1259357 (2014).
- 549 37 Schmidt, M. *et al.* Ligand migration pathway and protein dynamics in myoglobin: a time-resolved
550 crystallographic study on L29W MbCO. *Proceedings of the National Academy of Sciences of the*
551 *United States of America* **102**, 11704-11709, doi:10.1073/pnas.0504932102 (2005).
- 552 38 Srajer, V. *et al.* Photolysis of the carbon monoxide complex of myoglobin: Nanosecond time-
553 resolved crystallography. *Science* **274**, 1726-1729, doi:10.1126/science.274.5293.1726 (1996).
- 554 39 Nogly, P. *et al.* Retinal isomerization in bacteriorhodopsin captured by a femtosecond x-ray laser.
555 *Science* **361**, 145+, doi:10.1126/science.aat0094 (2018).
- 556 40 Skopintsev, P. *et al.* Femtosecond-to-millisecond structural changes in a light-driven sodium
557 pump. *Nature* **583**, 314+ (2020).
- 558 41 Srajer, V. *et al.* Protein conformational relaxation and ligand migration in myoglobin: a
559 nanosecond to millisecond molecular movie from time-resolved Laue X-ray diffraction.
560 *Biochemistry* **40**, 13802-13815 (2001).
- 561 42 Toh, K. C., Stojkovic, E. A., van Stokkum, I. H. M., Moffat, K. & Kennis, J. T. M. Fluorescence
562 quantum yield and photochemistry of bacteriophytochrome constructs. *Physical Chemistry*
563 *Chemical Physics* **13**, 11985-11997, doi:10.1039/C1cp00050k (2011).
- 564 43 Yang, X., Ren, Z., Kuk, J. & Moffat, K. Temperature-scan cryocrystallography reveals reaction
565 intermediates in bacteriophytochrome. *Nature* **479**, 428-432, doi:10.1038/nature10506 (2011).

- 566 44 Speziale, S. *et al.* Sound velocity and elasticity of tetragonal lysozyme crystals by Brillouin
567 spectroscopy. *Biophysical journal* **85**, 3202-3213 (2003).
- 568 45 Gushchin, I. *et al.* Mechanism of transmembrane signaling by sensor histidine kinases. *Science*
569 **356**, doi:10.1126/science.aah6345 (2017).
- 570 46 Gustavsson, E. *et al.* Modulation of Structural Heterogeneity Controls Phytochrome
571 Photoswitching. *Biophysical journal* **118**, 415-421, doi:10.1016/j.bpj.2019.11.025 (2020).
- 572 47 Nogales, E. The development of cryo-EM into a mainstream structural biology technique. *Nature*
573 *methods* **13**, 24-27, doi:10.1038/nmeth.3694 (2016).
- 574 48 Poudyal, I., Schmidt, M. & Schwander, P. Single-particle imaging by x-ray free-electron lasers-
575 How many snapshots are needed? *Struct Dyn* **7**, 024102, doi:10.1063/1.5144516 (2020).
- 576 49 Sanchez, J. *et al.* High-resolution crystal structures of a myxobacterial phytochrome at cryo and
577 room temperatures. *Structural Dynamics* (**accepted**) (2019).
- 578 50 Sugahara, M. *et al.* Grease matrix as a versatile carrier of proteins for serial crystallography.
579 *Nature methods* **12**, 61-63 (2015).
- 580 51 Sugahara, M. *et al.* Hydroxyethyl cellulose matrix applied to serial crystallography. *Scientific*
581 *reports* **7**, 703, doi:10.1038/s41598-017-00761-0 (2017).
- 582 52 Kubo, M. *et al.* Nanosecond pump-probe device for time-resolved serial femtosecond
583 crystallography developed at SACLA. *J Synchrotron Radiat* **24**, 1086-1091,
584 doi:10.1107/S160057751701030x (2017).
- 585 53 Nango, E. *et al.* A three-dimensional movie of structural changes in bacteriorhodopsin. *Science*
586 **354**, 1552-1557 (2016).
- 587 54 Grunbein, M. L. & Nass Kovacs, G. Sample delivery for serial crystallography at free-electron
588 lasers and synchrotrons. *Acta Crystallogr D Struct Biol* **75**, 178-191,
589 doi:10.1107/S205979831801567X (2019).
- 590 55 Grunbein, M. L. *et al.* Illumination guidelines for ultrafast pump-probe experiments by serial
591 femtosecond crystallography. *Nature methods*, doi:10.1038/s41592-020-0847-3 (2020).
- 592 56 Pande, K. *et al.* Femtosecond Structural Dynamics Drives the Trans/Cis Isomerization in
593 Photoactive Yellow Protein. *Science* **352**, 725-729 (2016).
- 594 57 Barends, T. R. *et al.* Direct observation of ultrafast collective motions in CO myoglobin upon
595 ligand dissociation. *Science*, doi:10.1126/science.aac5492 (2015).
- 596 58 Hutchison, C. D. M. *et al.* Photocycle populations with femtosecond excitation of crystalline
597 photoactive yellow protein. *Chem Phys Lett* **654**, 63-71, doi:10.1016/j.cplett.2016.04.087 (2016).
- 598 59 Shimazu, Y. *et al.* High-viscosity sample-injection device for serial femtosecond crystallography
599 at atmospheric pressure. *J Appl Crystallogr* **52**, 1280-1288 (2019).

- 600 60 Kameshima, T. *et al.* Development of an X-ray pixel detector with multi-port charge-coupled
601 device for X-ray free-electron laser experiments. *Review of Scientific Instruments* **85**,
602 doi:10.1063/1.4867668 (2014).
- 603 61 Nakane, T. *et al.* Data processing pipeline for serial femtosecond crystallography at SACLA. *J*
604 *Appl Crystallogr* **49**, 1035-1041, doi:10.1107/S1600576716005720 (2016).
- 605 62 Barty, A. *et al.* Cheetah: software for high-throughput reduction and analysis of serial
606 femtosecond X-ray diffraction data. *J Appl Crystallogr* **47**, 1118-1131, doi:Doi
607 10.1107/S1600576714007626 (2014).
- 608 63 White, T. A. *et al.* Recent developments in CrystFEL. *J Appl Crystallogr* **49**, 680-689,
609 doi:10.1107/S1600576716004751 (2016).
- 610 64 Winn, M. D. *et al.* Overview of the CCP4 suite and current developments. *Acta Crystallogr D* **67**,
611 235-242, doi:10.1107/S0907444910045749 (2011).
- 612 65 Schmidt, M. Time-Resolved Macromolecular Crystallography at Pulsed X-ray Sources.
613 *International Journal of Molecular Sciences* **20**, doi:<https://doi.org/10.3390/ijms20061401>
614 (2019).
- 615 66 Srajer, V. *et al.* Extraction of accurate structure-factor amplitudes from Laue data: wavelength
616 normalization with wiggler and undulator X-ray sources. *J Synchrotron Radiat* **7**, 236-244,
617 doi:10.1107/S0909049500004672 (2000).
- 618 67 Henderson, R. & Moffat, K. The difference Fourier technique in protein crystallography: errors
619 and their treatment. *Acta Crystallogr B* **27**, 1414-1420 (1971).
- 620 68 Pandey, S. *et al.* Time-resolved serial femtosecond crystallography at the European XFEL.
621 *Nature methods* **17**, 73-78, doi:10.1038/s41592-019-0628-z (2020).
- 622 69 Pettersen, E. F. *et al.* UCSF chimera - A visualization system for exploratory research and
623 analysis. *Journal of computational chemistry* **25**, 1605-1612, doi:10.1002/Jcc.20084 (2004).
- 624
- 625
- 626
- 627
- 628

629 **Acknowledgements**

630 This work was supported by National Science Foundation (NSF) Science and Technology Centers (STC)
631 grant NSF-1231306 (“Biology with X-ray Lasers”). Some results shown are derived from work performed
632 at Argonne National Laboratory, Sector 14 - BioCARS at the Advanced Photon Source. Argonne is
633 operated by UChicago Argonne, LLC, for the U.S. Department of Energy, Office of Biological and
634 Environmental Research under contract DE-AC02-06CH11 357. The experiments at SACLA were
635 performed at BL2 with the approval of the Japan Synchrotron Radiation Research Institute (JASRI)
636 (Proposal No. 2018A8055 and 2019A8007). EAS was supported by NSF-MCB-RUI 1413360, NSF-MCB-
637 EAGER grant 1839513 and NSF STC BioXFEL center award 6227. MN and LA training was supported in
638 part by the National Institute of General Medical Sciences (NIGMS) of the National Institutes of Health
639 (NIH) Maximizing Access to Research Careers (MARC) -T34 GM105549 grant. Use of BioCARS was
640 supported by NIH NIGMS under grant number P41 GM118217. This research is partially supported by
641 Platform Project for Supporting Drug Discovery and Life Science Research (Basis for Supporting
642 Innovative Drug Discovery and Life Science Research (BINDS)) from Japan Agency for Medical Research
643 and Development (AMED)). Structural models as well as structure factor amplitudes were deposited in the
644 Protein Data Bank with accession codes 7JR5 and 7JRI for the wild-type 5ns and 33 ms structures of
645 *SaBphP2* PCM, respectively.

646 **Author Contributions**

647 Conceptualization, E.A.S. and M.S.; Methodology, S.W., E.A.S. and M.S.; Samples, M.C., J.S., M.N.,
648 L.A., D.F. and E.A.S.; Data Collection, M.C., S.P., J.S., M.N., I.P., L.A., T.N.M., E. C., W. Y. W., D. F.,
649 V. Š., M.M., L.C., S.I., E.N., R.T., T.T., L.F., K.T., S.O., S.W., E.A.S. and M.S.; Data Processing: I.P.,
650 L.C. and S.P.; Data Analysis, S.P., E.A.S. and M.S.; Writing – Original Draft, E.A.S. and M.S.; Writing –
651 Review & Editing, E.A.S. and M.S. with input from all authors.; Funding Acquisition, S.I., S.W., E.A.S.
652 and M.S.; Resources and Supervision, S.I., S.W., E.A.S. and M.S..

653 **Corresponding Authors**

654 Sebastian Westenhoff, Emina Stojkovic, Marius Schmidt

655 **Declaration of Interests**

656 The authors declare no competing interests.

657

658

659

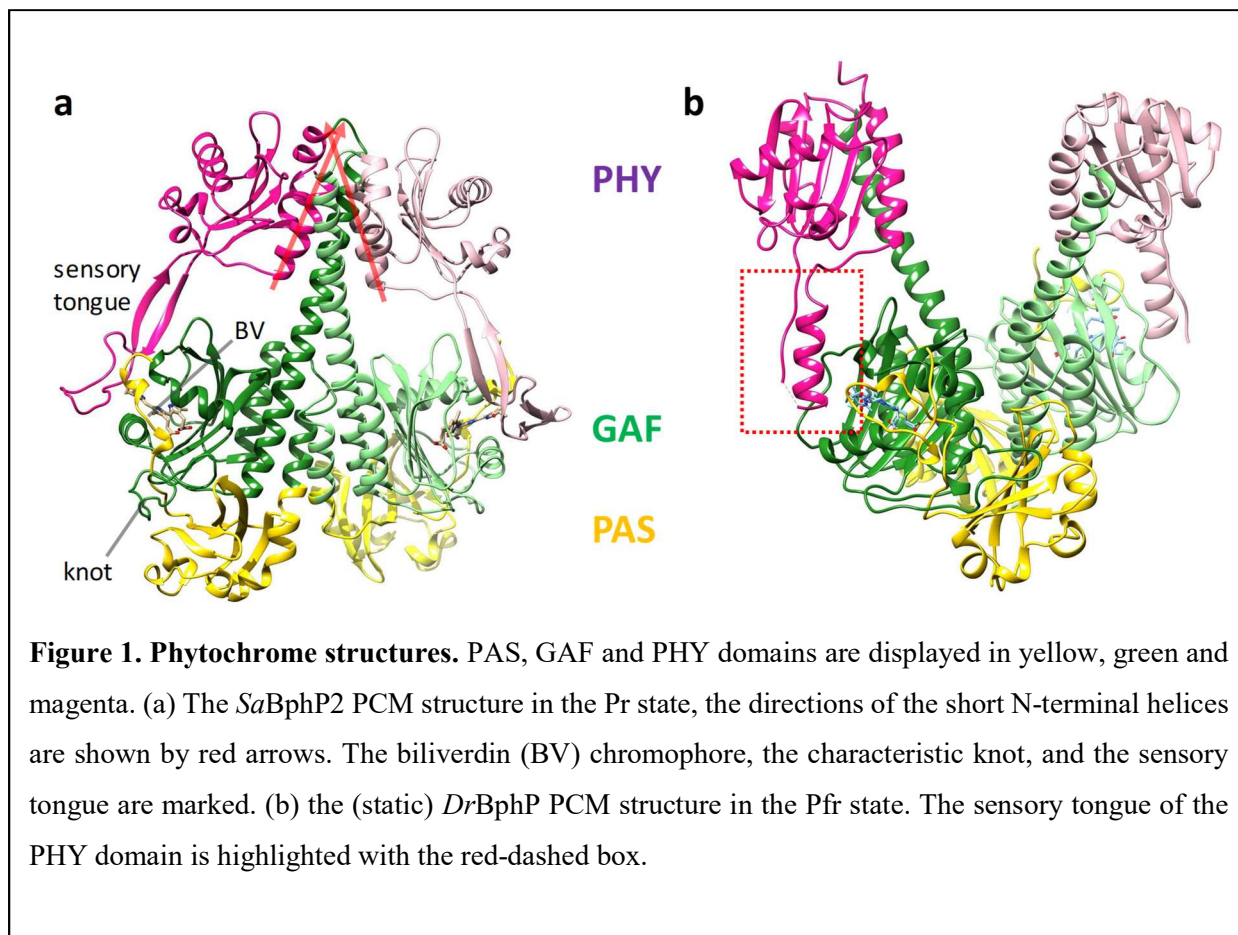
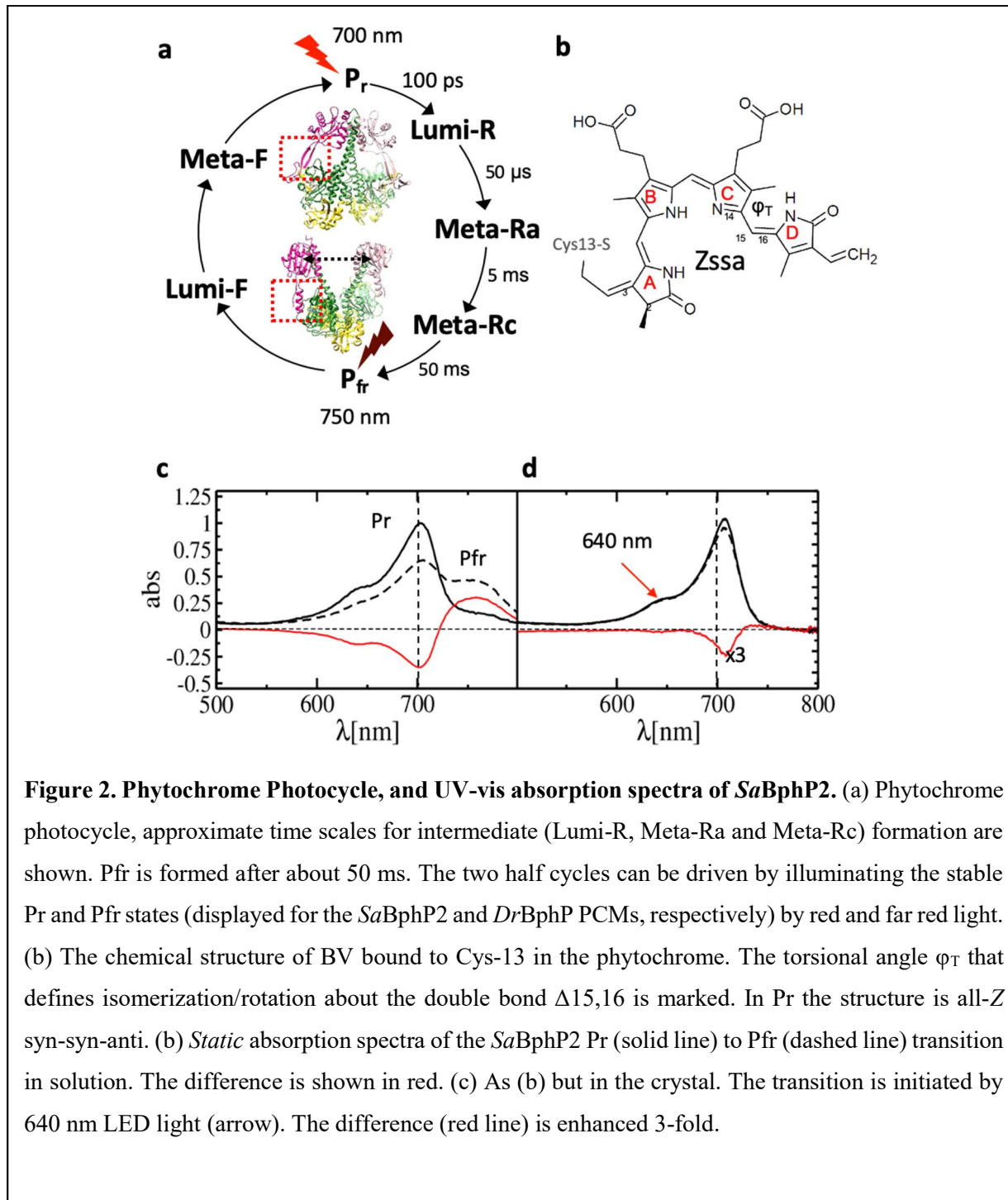


Figure 1. Phytochrome structures. PAS, GAF and PHY domains are displayed in yellow, green and magenta. (a) The *SaBphP2* PCM structure in the Pr state, the directions of the short N-terminal helices are shown by red arrows. The biliverdin (BV) chromophore, the characteristic knot, and the sensory tongue are marked. (b) the (static) *DrBphP* PCM structure in the Pfr state. The sensory tongue of the PHY domain is highlighted with the red-dashed box.

660

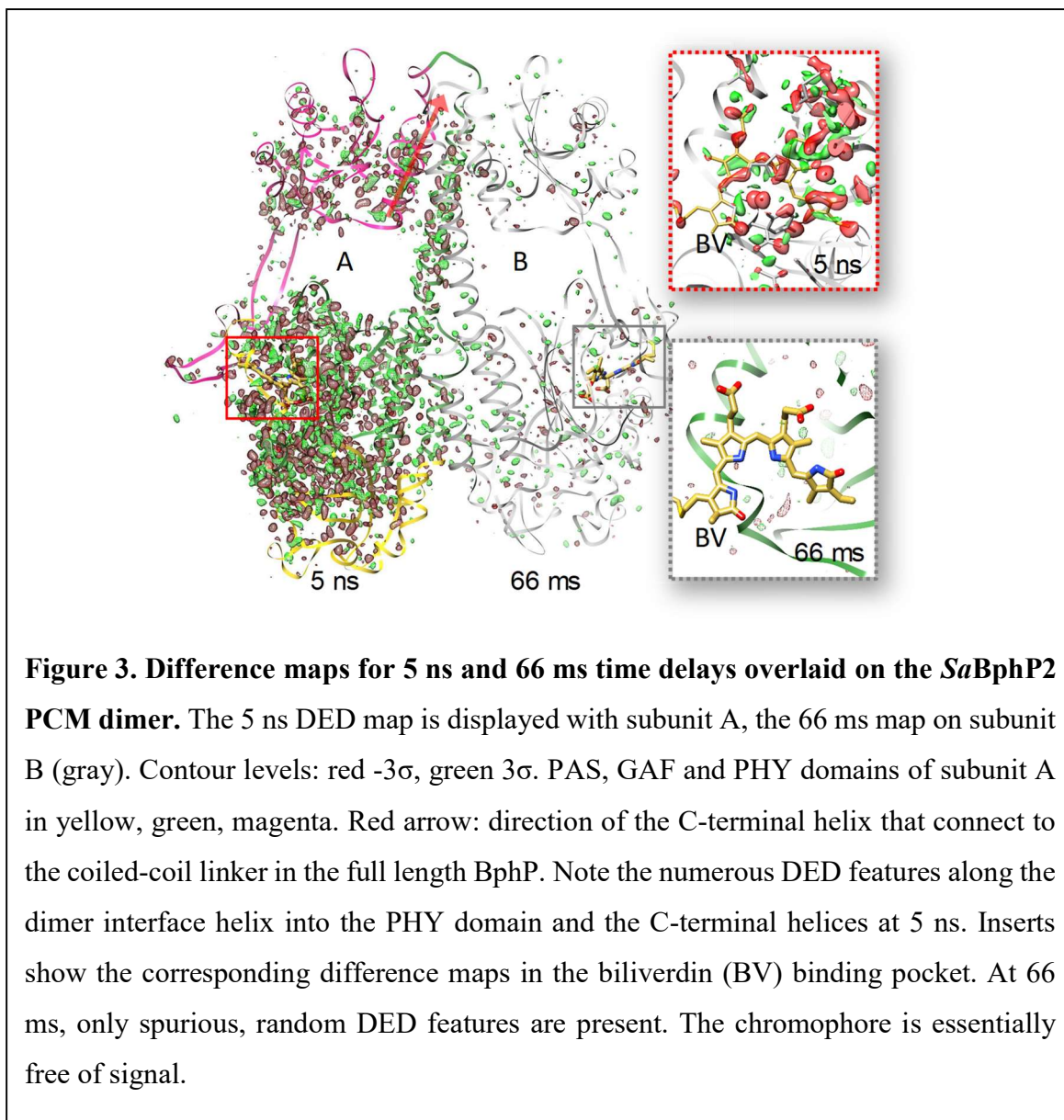
661

662



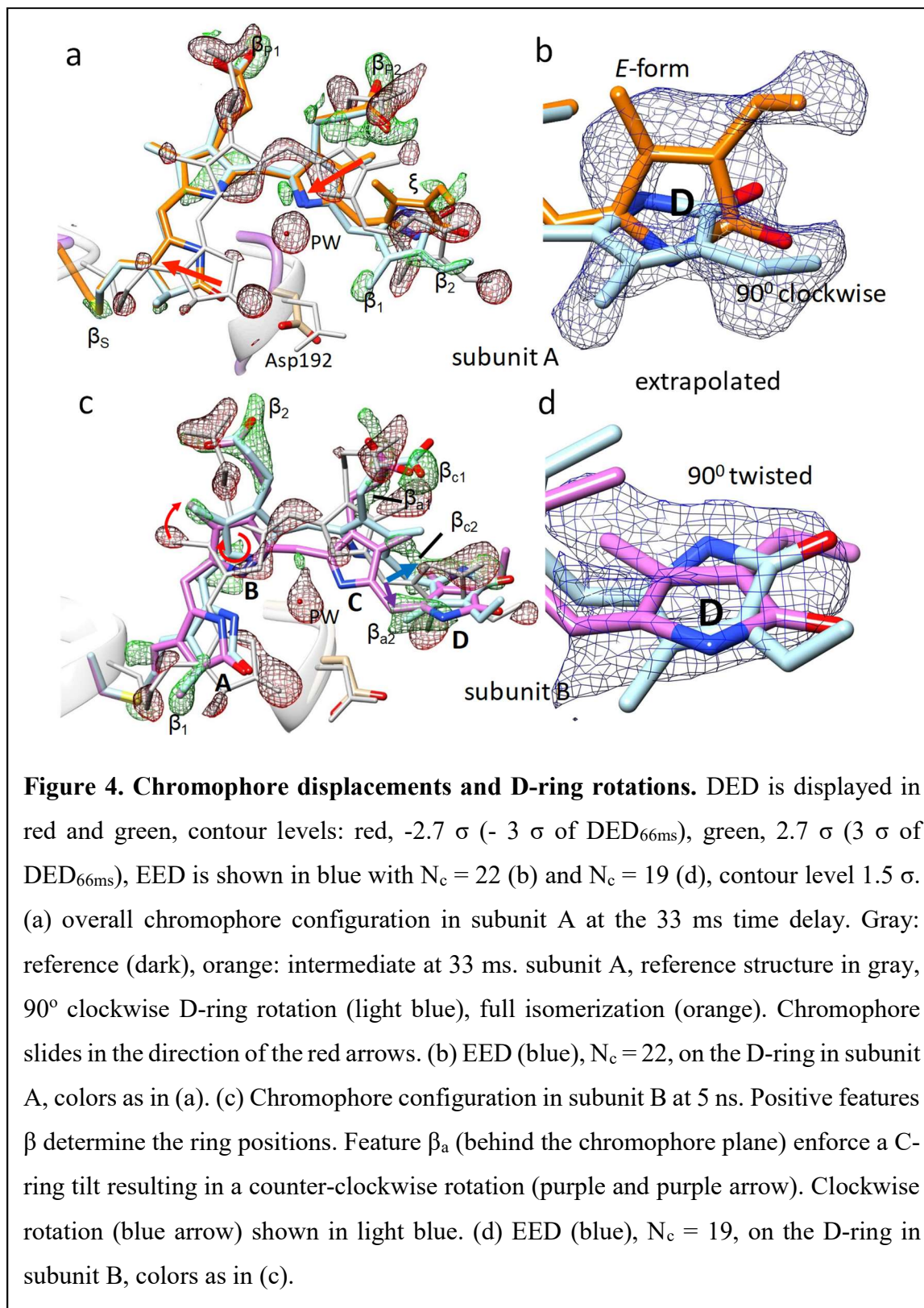
663

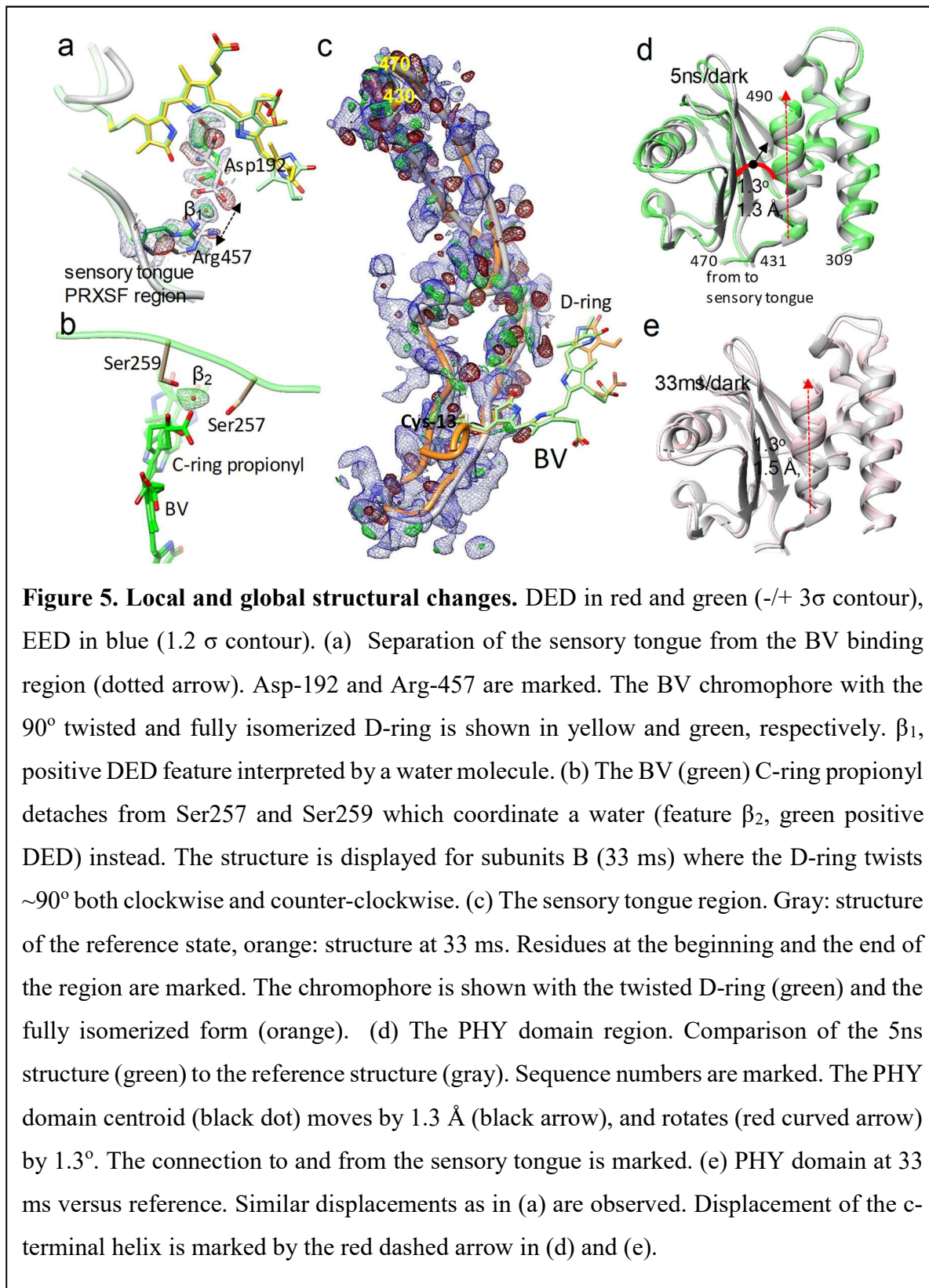
664



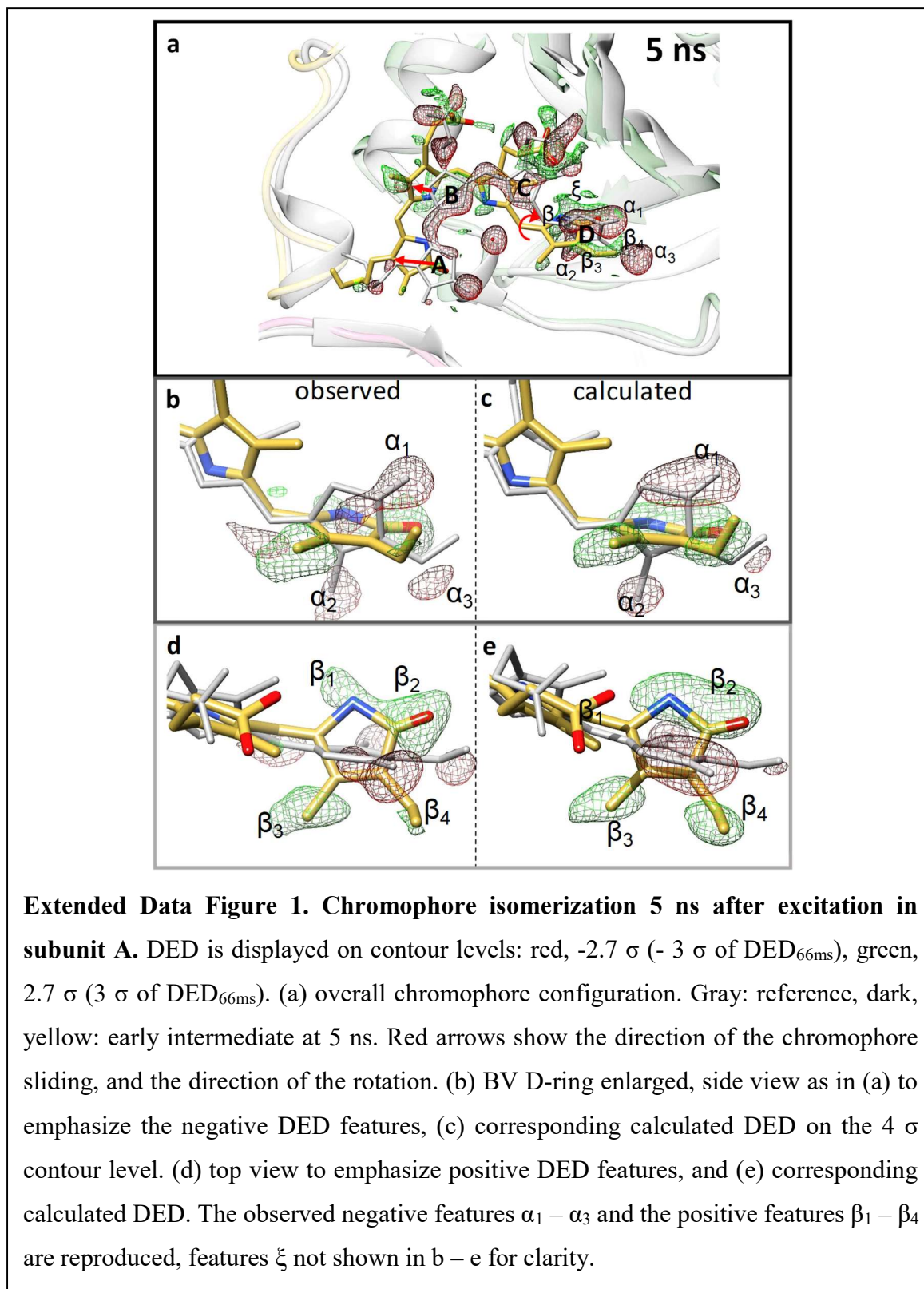
665

666





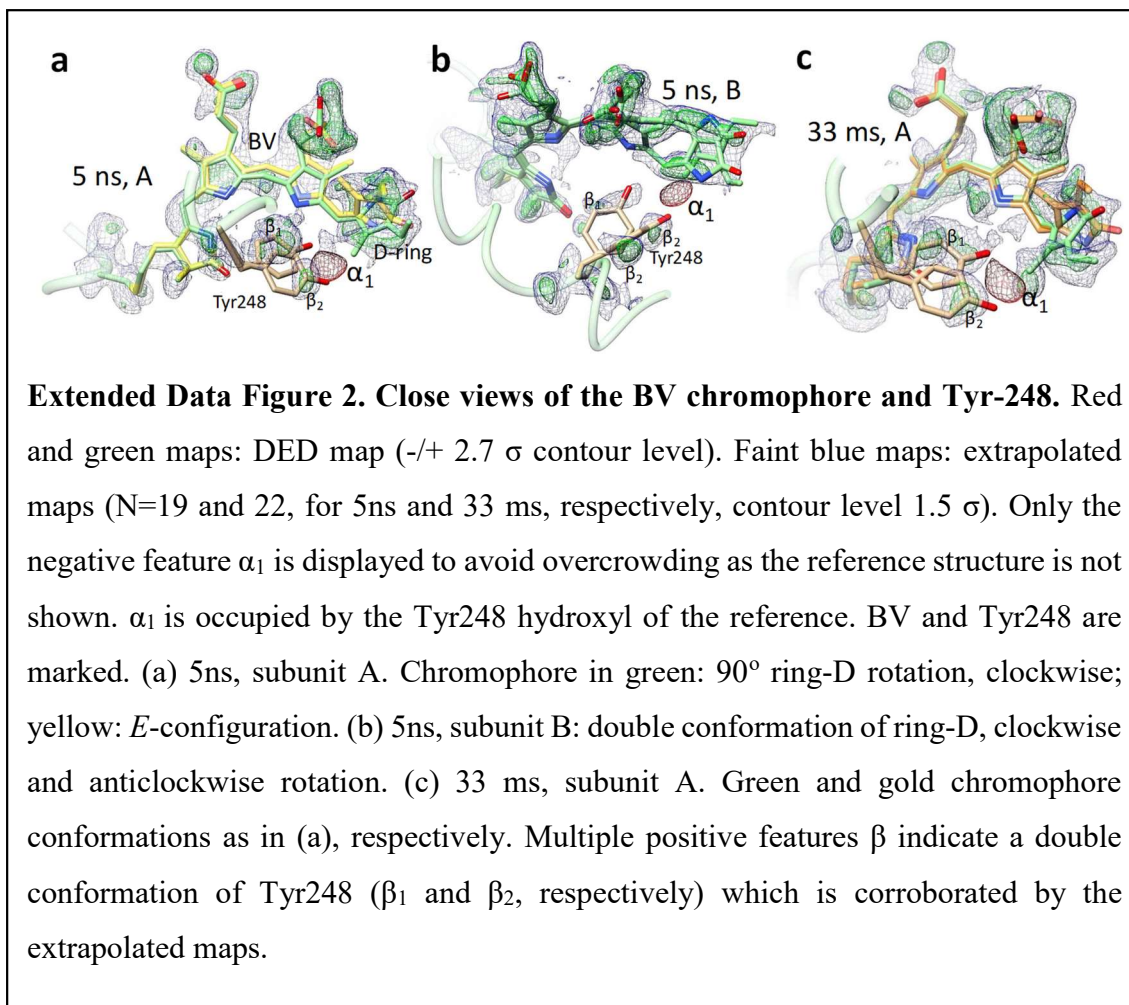
669 Extended Data Figures and Tables



671

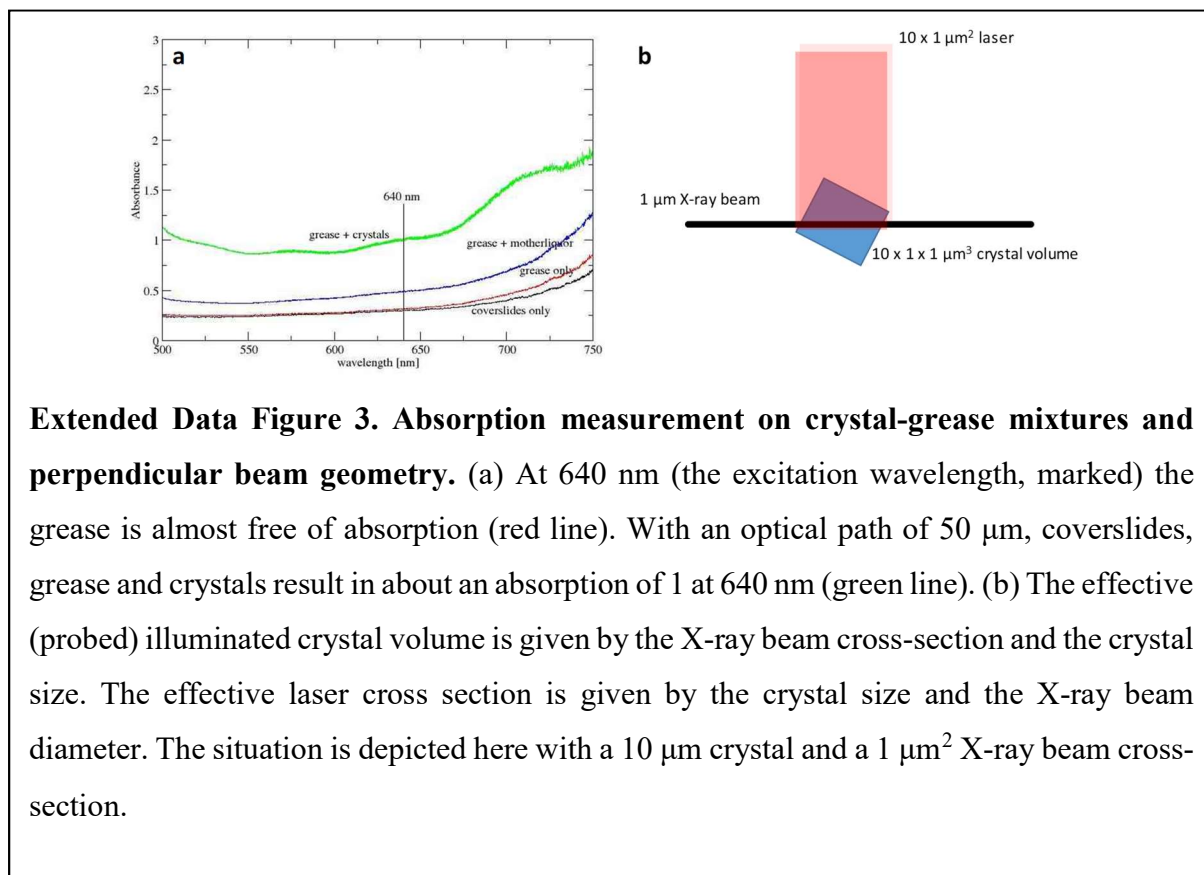
672

673



674

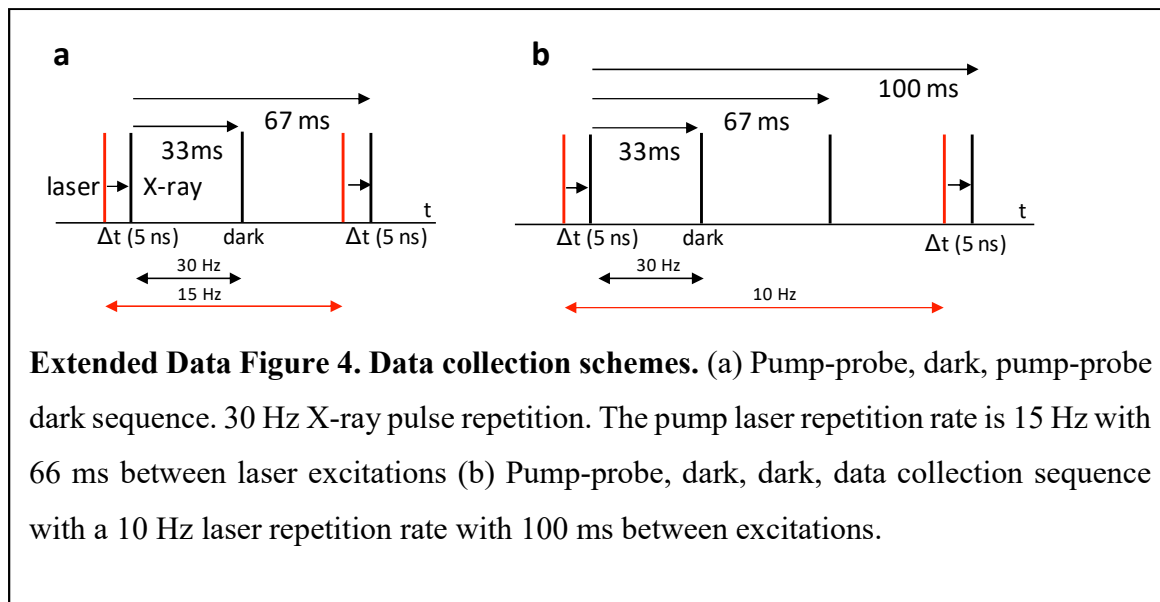
675



676

677

678

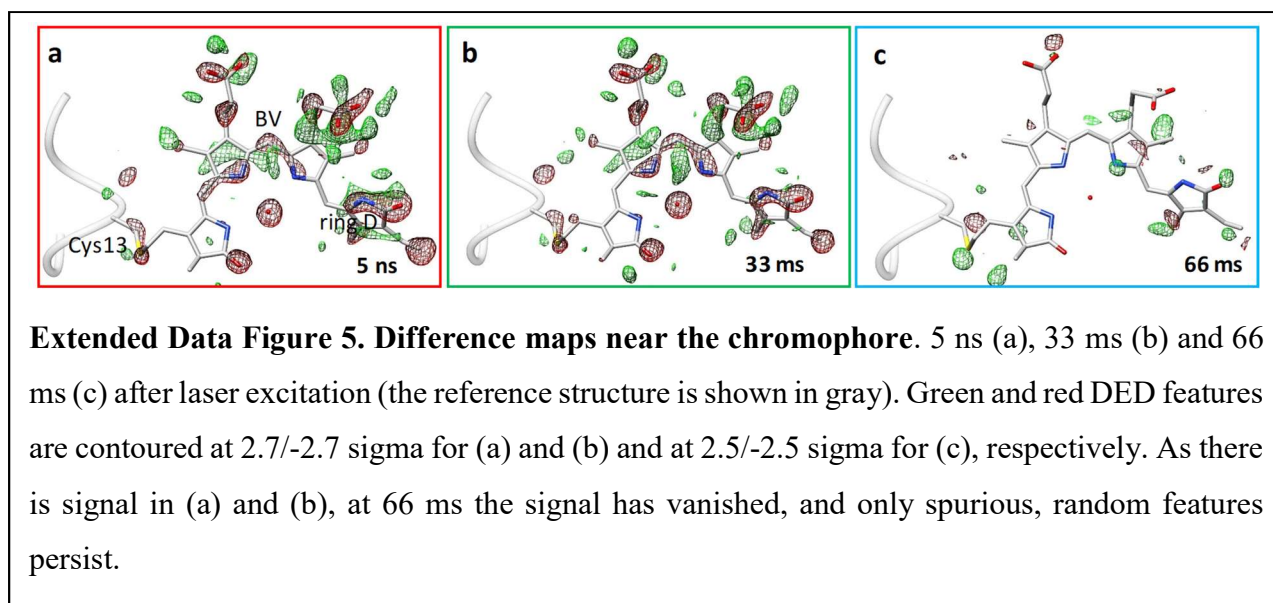


679

680

681

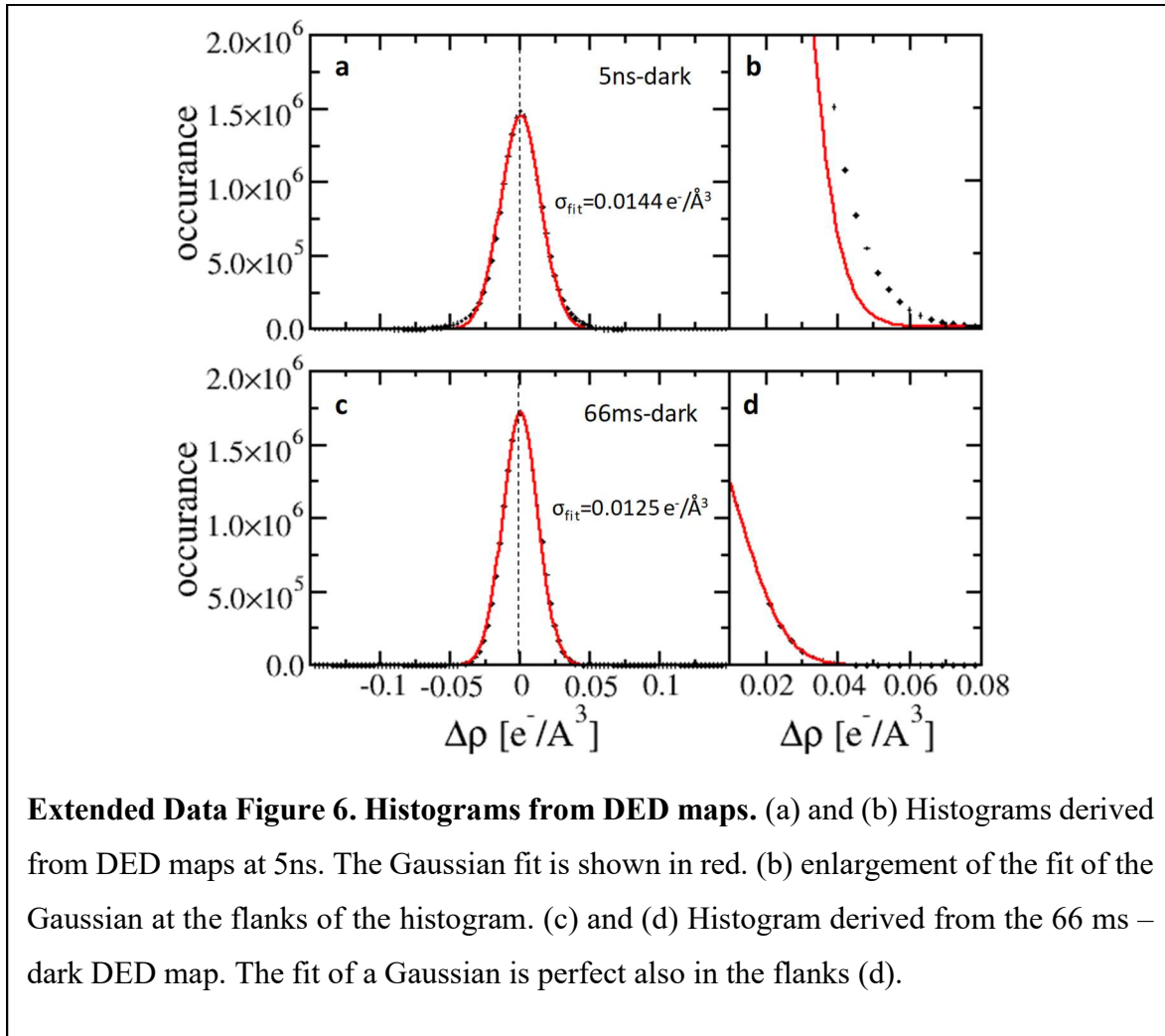
682



683

684

685



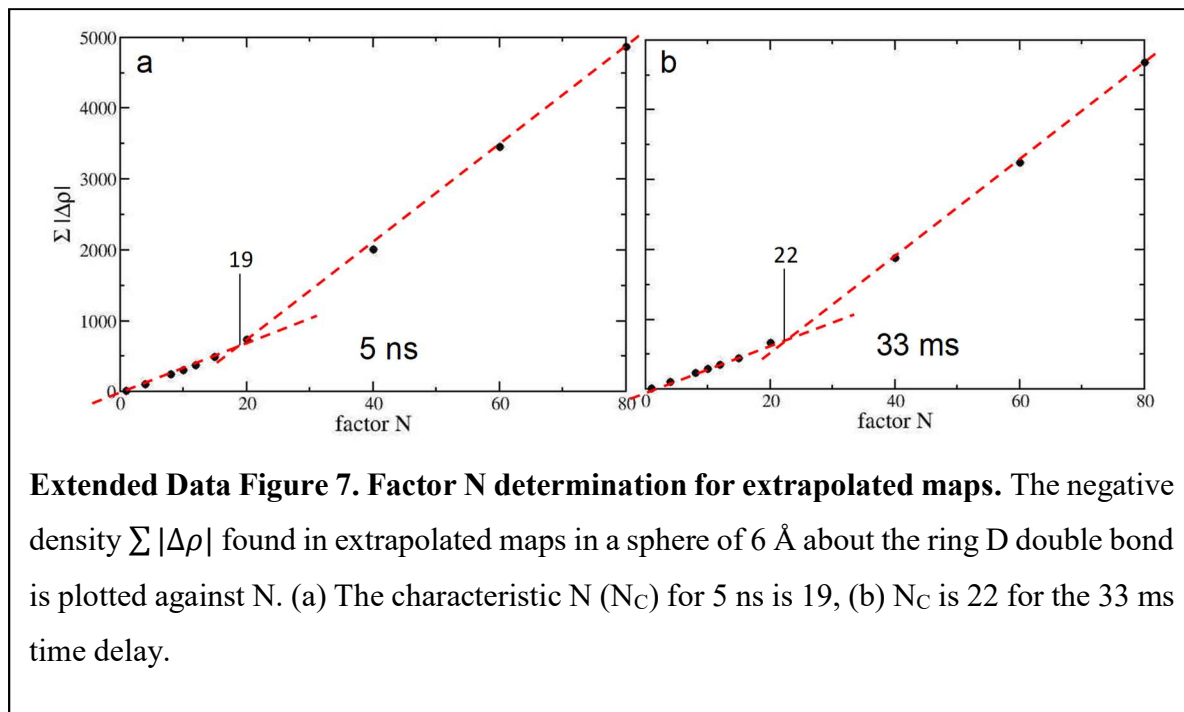
686

687

688

689

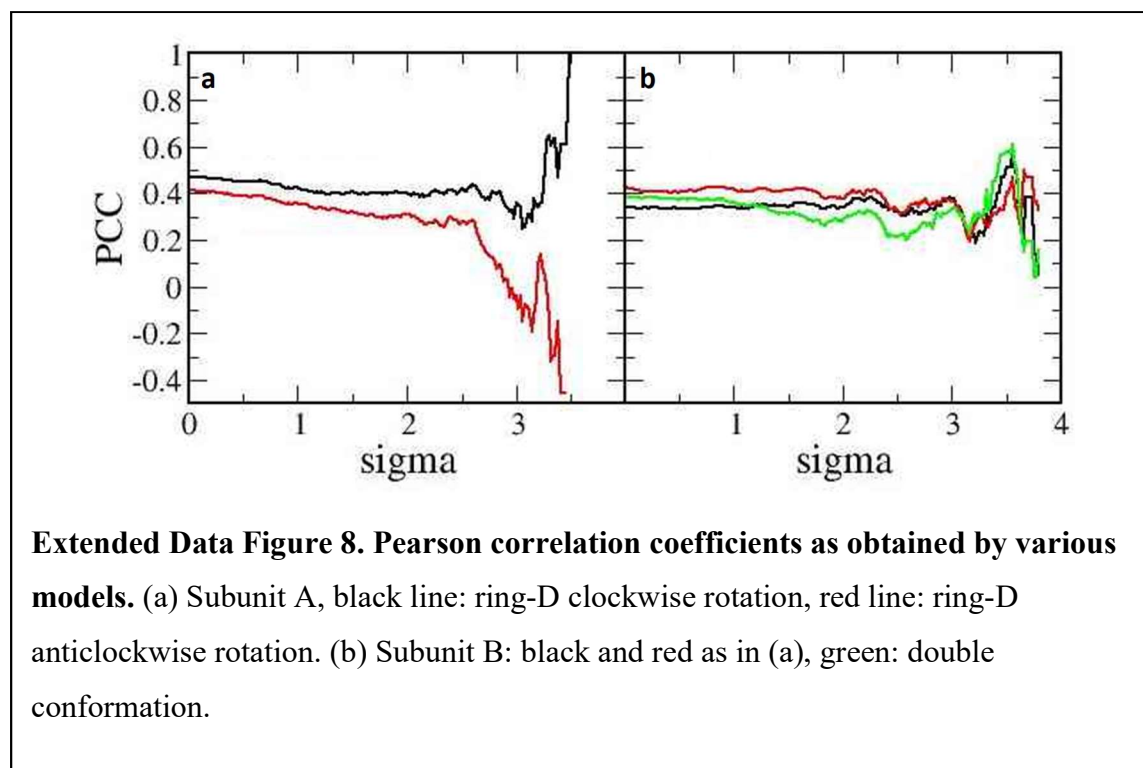
690



691

692

693



694

695

696

697

698

699 **Extended Data Table 1. Data collection statistics.**

700

	Dark	5 ns	33 ms	66 ms
Beamline	SACLA BL2			
Resolution	2.1 Å			2.3 Å
Temperature	285 K			
Space group	P2 ₁			
Unit-cell parameters (°,)	a = 83.7 Å b = 83.4 Å c=86.9 Å α=90° β=107.6° γ=90°			
Observations	35,170,843	30,128,819	30,917,561	10,193,417
No of unique reflections	68,911	68,919	68,919	53,717
Redundancy	510 (111)	437 (135)	449 (154)	190 (124)
Completeness (%)	100.0	100.0	100	100
CC1/2 at d _{min}	0.11	0.16	0.21	0.31
R _{split} (%)	11.1 (221.9)	9.4 (109.4)	9.4 (101.6)	18.1 (157.2)
Max/min Δρ	reference	7.0/-8.6	6.7/-8.6	5.2/-4.9
R _{cryst} /R _{free} (%)	19.5/23.7	31.4/34.1	29.3/33.3	--
D-ring torsion	32°/26°	A: -60°/-151° B: 134°/-88°	A: -52°/-160° B: 132°/-100°	--
RMSD to reference [Å]	n/a	1.4	1.5	--

701

702

703 **Extended Data Table 2. Difference electron density features and displacements.** Values are listed for
 704 selected functional groups and atoms at the 5 ns time-delay. If applicable, displacements are averaged over
 705 double conformations.

	Prominent DED Features, 5 ns		Displacements [\AA]	
	Subunit A Negative/positive [sigma]	Subunit B Negative/positive [sigma]	5ns	
			Subunit A	Subunit B
A-ring carbonyl	-5.5 / 3.5	-7.3 / n.o.	1.3	1.6
B-ring methyl	-3.4/2.8	-3.3/4.3	1.4	1.5
B-ring nitrogen	-4.5/3.7	-4.0/4.0	0.7	1.2
B-ring propionate carboxyl	-5.4/4.6	-5.4/5.0	1.5	1.5
C-ring propionate carboxyl	-6.1/3.9	-7.0/7.0	1.3	1.3
D-ring carbonyl	-8.5/3.8	-6.6/3.9	2.0	1.8
D-ring methyl	-4.0/3.4	-5.7/4.3	3.5	2.4
D-ring vinyl (double bond)	-3.3/3.2	-3.7/2.5	3.1	2.2
D-ring nitrogen	-5.3/3.2	-3.1/3.5	3.4	2.3
Tyr-201-OH	-6.0/4.2	-5.8/4.8	1.4	1.3
Tyr-248-OH	-5.5/4.1	-5.5/3.0	1.3	2.0
Ser-257-OG	-5.9/4.2	-6.1/3.7	1.6	1.4
Ser-259-OG	-4.6/4.0	-5.0/3.5	1.2	2.5
Ser-261-OG	-5.4/3.3	-6.3/4.0	1.8	1.0
Pyrrole water*	-6.1	-5.4	ex	ex

706 * photo-dissociated from binding pocket

707 n/o: not observed (positive and negative DED cancel)

708

709

710 **Extended Data Table 3. Observed DED features and expected random DED features.** Random features
 711 were estimated as a function of a multiple (x) of sigma (sigma level) in the unit cell of the *SaBphP2*
 712 difference map calculated on a 88 x 88 x 88 grid (N = 681472). The number of observed peaks was
 713 determined by the ccp4 program *peakmax* as a function of the DED sigma value. PM is the probability to
 714 observe at least one random feature equal or more than a given sigma level in the *entire* map, as opposed
 715 to the probability PI to observe this random feature in an individual voxel. Note, we write (1 - erf) rather
 716 than using the equivalent erfc, where erf is the error-function.

Feature [sigma]	Observed	$\text{erf}(x/\sqrt{2})$	PI $1-\text{erf}(x/\sqrt{2})$	$\text{erf}(x/\sqrt{2})^N$	PM $1-\text{erf}(x/\sqrt{2})^N$	expected random features in the DED map $N * (1.0 - \text{erf}(x/\sqrt{2}))$
1	> 8000	0.68	0.31	0.0	1.0	216238
2	> 8000	0.95	0.05	0.0	1.0	31007
3	3167	0.997	0.002	0.0	1.0	1839
4	1018	1.0	0.0	0.0	1.0	43
5	264	1.0	0.0	0.67	0.33	0.4
6	44	1.0	0.0	1.0	0.0	0.0

717

718

719 **Extended Data Table 4. Comparison of the reference (dark) and the 5 ns and the 33 ms SaBphP2**
 720 **structures. Bold entries: important interactions. Bold numbers: large changes relative to the reference**
 721 **structure.**

	reference (Pr)		5 ns		33ms	
	A	B	A	B	A	B
Asp192-O/A-ring N	3.0	3.3	3.1/3.1	4.4/4.0	3.8/4.0	4.1/4.6
Asp192-O/A-ring carbonyl	4.5	4.4	4.1/4.1	5.5/5.8	4.5/5.1	5.4/5.6
Asp192-OD2/A-ring carbonyl	3.2	3.2	4.1/4.1	4.1/4.1	3.4/4.6	3.9/4.1
Asp192-O/B-ring N	3.0	3.0	2.9/3.0	3.1/3.3	4.2/4.3	3.3/3.3
Asp192-O/C-ring N	2.9	3.0	3.8/4.1	5.1/5.2	5.1/5.1	4.7/5.0
Asp192-OD2/Arg457-NH	2.6	2.9	5.4	3.0	4.4	4.8
Asp192-OD2/Tyr161-OH	5.6	5.7	5.5	4.9	5.6	4.2
Asp192-OD2/Tyr248-OH	2.7	2.7	3.5/3.5	5.8/5.3	5.3/5.5	3.9/4.4
Tyr248-OH/D-ring methyl	3.5	3.5	2.7/4.2	3.4/>5.0	2.6/3.9	2.9/5.3
Tyr248-OH/Arg457-NH1	4.2	4.4	3.5/> 5.0	3.5/4.3	5.3/5.5	4.8/5.5
Ser242-N/B-ring propionyl O2	2.9	2.8	5.1/5.1	4.3/>5.0	3.3/3.3	5.2/5.7
Ser257-OG/C-ring propionyl O2	3.2	2.5	2.3/2.6	2.6/ 3.9	2.6/ 3.3	3.5/5.0
Ser259-OG/C-ring propionyl O2	2.7	2.7	3.1/3.3	2.6/2.5	2.1/ 3.5	2.3/2.4
Ser259-OG/Arg207-NH2	2.9	2.8	5.1	4.7	4.4	5.4
His275-NE2/C-ring propionyl O2	4.7	6.2	6.0	7.1/7.2	6.7/6.9	6.2/7.5
His275-NE2/D-ring carbonyl	3.0	2.8	6.0	2.8/ 4.3	4.3/4.8	3.3/ 4.4
His275-ND1/Arg157-NH2	2.9	2.9	3.6	3.8	2.7/ 4.8	4.5
His245-ND1/B-ring N	3.5	3.6	3.6/3.8	3.7/3.8	3.7/3.7	5.1/5.3
His245-ND1/C-ring N	3.4	3.6	3.7/3.8	4.2/4.7	3.7/3.8	4.6/5.4
His245-NE2/C-ring propionyl O1	2.6	2.8	2.7	2.9/ 3.8	3.0/ 3.5	3.4/5.4
Arg457-NH1/A-ring carbonyl	4.5	4.5	6.0	5.4/5.5	7.4/7.4	7.0/7.2
Tyr201-OH/Arg207-NH1	4.0	3.9	3.7	4.0	4.9	3.0
Tyr201-OH/B-ring propionyl O1	2.7	2.8	2.9	2.7/3.1	2.8/2.9	2.3/3.1
Tyr201-OH/C-ring propionyl O1	5.9	5.9	4.4/5.9	5.0/5.0	5.9/6.1	5.7/5.7
Ser261-OG/ Arg207-NE	3.1	2.7	3.6	4.0	3.6	4.0
Arg207-NH2/C-ring propionyl O1	5.4	5.3	4.9/6.1	4.1/5.7	4.1/5.1	3.9/4.2
Arg239-NH2/B-ring propionyl O1	2.7	2.9	2.4	2.5/2.6	3.8/3.9	2.8/2.9
A-Ring torsion	7	9	12/20	40/40	7/-1	15/39
D-Ring torsion	32	27	-61/-151	134/-88	-62/-160	132/-100
B/C-Ring relative tilt*	11	14	25/25	43/37	32/46	43/46
Δ D-ring rotation**	-	-	-93/ -183	102/ -120	-94/ -192	105/ -127

722

723 * separately for the two alternate conformations

724 **difference between D-ring torsion in the dark and the D-ring torsion at measured time delays. **Negative**
 725 values: clockwise rotation relative to dark, **positive** values: counterclockwise rotation relative to dark,
 726 bold red: *E*-configuration.

727

728 **Extended Data Table 5. Important distances in other BphP structures** (identified by pdb entry).

729 Sequence numbers are in the *Sa*BphP2 PCM convention (directly comparable with Extended Data Tab.
730 4), they denote equivalent amino acid residues found in the various structures. L3 is an intermediate
731 determined by temperature scan crystallography.

	1ps 6TSU		<i>Dr</i> BphP (Pfr) 5C5K		Bathy <i>Pa</i> BphP (Pfr) 3C2W		L3 (bathy) 3NOU
	A	B	A	B	A	B	A
Asp192-O/A-ring N	2.7	3.2	2.8	2.8	3.2	3.1	3.0
Asp192-OD2/A-ring carbonyl	4.3	4.8	4.1	4.2	3.5	2.8	3.3
Asp 192-O/A-ring carbonyl	3.8	3.8	3.9	3.6	4.1	3.4	3.9
Asp192-O/B-ring N	3.0	3.4	3.1	3.3	3.1	3.6	2.7
Asp192-O/C-ring N	3.4	3.5	3.5	3.4	3.0	3.3	2.7
Asp192-OD2/Arg457-NH	n/a	n/a	16.1	15.8	nd	nd	nd
Asp192-OD2/Tyr248-OH	5.9	5.2	3.8	3.8	4.0	4.5	3.9
Tyr248-OH/D-ring carbonyl	4.1	4.0	3.5	3.1	3.2	3.9	N/A
Ser242-N/B-ring propionyl O2	3.2	3.3	4.9	4.7	5.1	4.8	5.5
Ser257-OG/C-ring propionyl O2	3.7	4.0	3.1	2.2	2.5	3.5	4.7
Ser259-OG/C-ring propionyl O2	4.5	3.6	6.8	3.9	6.7	6.2	2.5
Ser259-OG/Arg207-NH2	3.2	3.7	7.5	7.7	nd	nd	nd
His275-NE2/C-ring propionyl O2	5.4	5.7	3.8	5.0	2.8	3.4	4.1
His275-NE2/D-ring carbonyl	3.9	4.3	7.7	8.6	nd	nd	6.6
His275-ND1/Arg157-NH2	4.9	4.3	6.9	6.5	4.7	4.2	4.8
His245-ND1/B-ring N	3.6	3.5	3.6	4.5	3.7	3.7	4.2
His245-ND1/C-ring N	4.0	4.2	3.6	3.7	3.8	3.9	4.3
His245-NE2/C-ring propionyl O1	2.8	2.7	2.8	3.7	4.2	4.2	5.6
Tyr201-OH/Arg207-NH	4.7	4.4	7.5	7.2	nd	nd	nd
Tyr201-OH/B-ring propionyl O1	2.7	3.8	3.8	3.1	3.8	2.8	2.8
Tyr201-OH/C-ring propionyl O1	7.3	6.0	5.7	3.3	5.4	5.1	2.9
Ser261-OG/ Arg207-NH1	2.7	2.8	nd	nd	nd	nd	nd
Arg239-NH2/B-ring propionyl O1	3.4	3.0	3.5	2.7	4.0	4.1	4.6
Ring-A torsion	19	40	-7	10	11	30	24
Ring-D torsion	58	89	-142	-161	-150	-143	-25***
B/C-Ring relative tilt	8	9	0	0	5	6	35
Δ ring D rotation	33*	69*	-179**	-198**	na	na	125

732 *difference from comparing pdb entries 6TSU/6T31, **counterclockwise** rotation (positive)

733 ** difference from comparing pdb entries 5C5K/4Q0J, **clockwise** rotation (negative)

734 *** bathy phytochrome: -150° in the dark, rotation relative to dark is **counterclockwise** (positive)

735 nd: not done, n/a not applicable because the residue is missing.